



BRNO UNIVERSITY OF TECHNOLOGY

VYSOKÉ UČENÍ TECHNICKÉ V BRNĚ

FACULTY OF ELECTRICAL ENGINEERING AND COMMUNICATION

FAKULTA ELEKTROTECHNIKY
A KOMUNIKAČNÍCH TECHNOLOGIÍ

DEPARTMENT OF POWER ELECTRICAL AND ELECTRONIC ENGINEERING

ÚSTAV VÝKONOVÉ ELEKTROTECHNIKY A ELEKTRONIKY

DESIGN OF SYNCHRONOUS RELUCTANCE MOTOR WITH PERMANENT MAGNETS

NÁVRH SYNCHRONNÍHO RELUKTANČNÍHO MOTORU S PERMANENTNÍMI MAGNETY

MASTER'S THESIS
DIPLOMOVÁ PRÁCE

AUTHOR
AUTOR PRÁCE

Bc. Ladislav Knebl

SUPERVISOR
VEDOUCÍ PRÁCE

doc. Ing. Čestmír Ondrůšek, CSc.

BRNO 2017



Diplomová práce

magisterský navazující studijní obor **Silnoproudá elektrotechnika a výkonová elektronika**

Ústav výkonové elektrotechniky a elektroniky

Student: Bc. Ladislav Knebl

ID: 159186

Ročník: 2

Akademický rok: 2016/17

NÁZEV TÉMATU:

Návrh synchronního reluktančního motoru s permanentními magnety

POKYNY PRO VYPRACOVÁNÍ:

1. Proveďte literární průzkum dané problematiky.
2. Navrhněte synchronní reluktanční motor 6,7 Nm, 2450ot/min s permanentními magnety.
3. Proveďte srovnání vypočtených výsledků metodou koeficientů s analytickým výpočtem.
4. Porovnejte vypočtené hodnoty s měřením na vyrobeném motoru.

DOPORUČENÁ LITERATURA:

- [1] Cigánek, L., Bauer, M.: Elektrické stroje a přístroje
- [2] Fitzgerald, A.E., Kingsley, Ch., Kusko, A.: Electric machinery. McGraw Hill 1971
- [3] Měřička, J., Zoubek, Z.: Obecná teorie elektrického stroje SNTL 1973
- [4] Chee-Mu Ong,: Dynamic simulation of electric machinery. Prentice Hall 1998
- Pyrhonen, J., Jokinen, T., Hrabovcová, V.: Design of rotating electrical machines, 2010

Termín zadání: 6.2.2017

Termín odevzdání: 24.5.2017

Vedoucí práce: doc. Ing. Čestmír Ondrůšek, CSc.

Konzultant:

doc. Ing. Ondřej Vítek, Ph.D.
předseda oborové rady

UPOZORNĚNÍ:

Autor diplomové práce nesmí při vytváření diplomové práce porušit autorská práva třetích osob, zejména nesmí zasahovat nedovoleným způsobem do cizích autorských práv osobnostních a musí si být plně vědom následků porušení ustanovení § 11 a následujících autorského zákona č. 121/2000 Sb., včetně možných trestněprávních důsledků vyplývajících z ustanovení části druhé, hlavy VI. díl 4 Trestního zákoníku č.40/2009 Sb.

Abstrakt

V dnešní době je kladen vysoký nárok na účinnost elektrických zařízení a to jak ze strany provozovatele, tak i legislativy. Nejlepší účinnosti dosahují synchronní motory s permanentními magnety umístěnými na povrchu rotoru (SMPM), se kterými lze i u malých motorů dosáhnout účinnosti nad 90%. Nicméně tyto motory jsou z důvodů použití magnetů ze vzácných zemin, např. NdFeB, drahé a jsou schopny provozu pouze s frekvenčním měničem. Z cenových důvodů jsou hledány levnější alternativy k SMPM motorům. Jedním z typů motorů, kterým lze SMPM nahradit je synchronní reluktanční motor s permanentními magnety (PMASR). Tento motor je cenově výhodnější, protože používá menší množství magnetů, při zachování podobných, mnohdy i lepších vlastností, nicméně neodpadá potřeba použití frekvenčního měniče. Navíc je zde možnost použití levnějších feritových magnetů a tím ještě výrazněji snížit cenu motoru. V této práci bude PMASR topologie popsána důkladněji včetně elektromagnetického návrhu metodou konečných prvků. Bude provedena i mechanická analýza zvoleného optimálního modelu. Výsledky dosažené metodou konečných prvků budou následně porovnány s analytickým modelem. Z navrženého modelu bude vyroben prototyp a naměřené výsledky budou porovnány s výpočty.

Klíčová slova

PMASR, design, feritové magnety, neodymiové magnety, analytický model, odporová síť, ustálený stav, bariéra toku, magnetický odpor, magnetická nesymetrie, anisotropický motor, MKP, Matlab, FEMAG, LUA script, mechanická analýza, Ansys, prototyp, vysoká teplota, vyřezávání laserem, degradované železo, žíhání

Abstract

In these days a huge emphasis is put on efficiency of electric devices, both from the side of the owner as well as from the legislation. In the case of electric motors the best efficiency can be achieved with a surface mounted permanent magnet (SMPM) motor, which may be, even in the case of small machines, higher than 90%. Unfortunately, these motors are expensive, because rare earth magnets, such as neodymium magnets, are used, and use of the AC drive system is required. Because of its high price, engineers are trying to find a cheaper machine with parameters similar to SMPM solution. Permanent magnet assisted synchronous reluctance (PMASR) motor is one possible replacement for SMPM. This machine is cheaper, because smaller amount of magnets and still similar or even better characteristics could be achieved, but still the AC drive needs to be used. With PMASR topology it is possible to use low-cost ferrite magnets to replace expensive neodymium magnets, thus the machine will be cheaper. In this work, there will be PMASR topology explained more thoroughly, including the electromagnetic design process. Analytical analysis will be performed on a chosen optimal model. Results of the FE analysis will be evaluated with the analytical model. The prototype will be manufactured from the optimal designed model. The measured data from the prototype will be compared with the calculated data.

Keywords

PMASR, design, ferrite magnets, neodymium magnets, analytical model, reluctance network, stable state, flux barrier, reluctance, magnetic saliency, anisotropic rotor, FEA, Matlab, FEMAG, LUA script, mechanical analysis, Ansys, prototype, high temperature, laser cutting, degraded iron, annealing

Bibliografická citace:

KNEBL, L. Návrh synchronního reluktančního motoru s permanentními magnety. Brno: Vysoké učení technické v Brně, Fakulta elektrotechniky a komunikačních technologií, 2017. 68 s. Vedoucí diplomové práce doc. Ing. Čestmír Ondrůšek, CSc

Prohlášení

„Prohlašuji, že svou závěrečnou práci na téma “Návrh synchronního reluktančního motoru s permanentními magnety” jsem vypracoval samostatně pod vedením vedoucího diplomové práce a s použitím odborné literatury a dalších informačních zdrojů, které jsou všechny citovány v práci a uvedeny v seznamu literatury na konci práce.

Jako autor uvedené závěrečné práce dále prohlašuji, že v souvislosti s vytvořením této závěrečné práce jsem neporušil autorská práva třetích osob, zejména jsem nezasáhl nedovoleným způsobem do cizích autorských práv osobnostních a jsem si plně vědom následků porušení ustanovení § 11 a následujících autorského zákona č. 121/2000 Sb., včetně možných trestněprávních důsledků vyplývajících z ustanovení části druhé, hlavy VI. díl 4 Trestního zákoníku č. 40/2009 Sb.

V Brně dne **24. května 2017**

.....
podpis autora

Poděkování

Děkuji vedoucímu diplomové práce doc. Ing. Čestmíru Ondrůškovi Csc. za účinnou metodickou, pedagogickou a odbornou pomoc a další cenné rady při zpracování mé diplomové práce.

Děkuji i panu Ing. Jiřímu Kurfürstovi PhD. za vřelý přístup, odbornou pomoc a vedení při zpracování mé diplomové práce.

V neposlední řadě bych chtěl poděkovat Ježíši Kristu, za umožnění studia dodávání sil a zprostředkování všech potřebných věcí vedoucích k úspěšnému napsání tohoto dokumentu a prohloubení vztahu s ním.

Dále bych chtěl poděkovat rodině za finanční zabezpečení mých studií i morální podporu v celém průběhu studia.

V Brně dne **24. května 2017**

.....
podpis autora(-ky)

Content

1 Introduction.....	2
2 PERMANENT MAGNET ASSISTED SYNCHRONOUS RELUCTANCE MOTOR.....	3
2.1 What is the PMASR	3
2.2 Why PMASR?	4
2.3 Fundamental equations	4
2.4 Mathematic definition of PMASR	6
2.5 PMASR in stable state	8
3 Analytical model of PMASR	10
3.1 Introduction	10
3.2 Stator analytical model	10
3.2.1 Electric loading	10
3.2.2 Magnetic potential.....	11
3.3 Analytical model of rotor with one flux barrier per pole	12
3.3.1 Magnetic potential.....	12
3.3.2 Magnetic torque computation	15
3.4 Analytical model of rotor with two flux barriers per pole	16
3.4.1 Rotor magnetic potential.....	17
3.4.2 Torque calculation.....	20
4 FEA Model	22
4.1 Introduction	22
4.2 Finite element method	22
4.3 Software.....	22
4.4 Scripts	23
5 Motor design.....	27
5.1 Introduction	27
5.2 SRAM1 geometry, $Q=12, 2p=10$	27
5.2.1 SRAM1 12/10 combination with one flux barrier per pole geometry	28
5.2.2 SRAM1 12/10 combination with two flux barriers per pole geometry ..	28
5.3 SRAM1 geometry, $Q=27, 2p= 6$	29
5.3.1 SRAM1 27/6 combination with one flux barrier per pole geometry.....	30
5.3.2 SRAM1 27/6 combination with two flux barriers per pole geometry	30
5.3.3 SRAM1 27/6 combination with three flux barriers per pole geometry ..	31
5.4 SRAM1 geometry, $Q=36, 2p= 8$	31
5.4.1 SRAM1 36/8 combination with one flux barrier per pole geometry.....	32
5.4.2 SRAM1 36/8 combination with two flux barriers per pole geometry	32
5.4.3 SRAM1 36/8 combination with three flux barriers per pole geometry ..	32
5.5 SRAM2 geometry, $Q_s = 36, 2p= 8$	34

5.5.1 SRAM2 36/8 combination with two flux barriers per pole geometry	34
5.6 SRAM3 geometry, $Q_s = 36$, $2p = 8$	37
5.7 Comparison of the geometries	39
6 Mechanical analysis	42
6.1 Introduction	42
6.2 Static structural analysis	42
6.3 Setup	43
6.4 Mechanical analysis summary	44
7 FEA and analytical model Comparison	45
7.1 Introduction	45
8 FEA and prototype comparison	47
8.1 Results comparison	47
8.2 MMF harmonics in permanent magnets	48
8.3 Laser cutting influence on magnetic properties	49
9 Conclusion	51
Bibliography	53
List of symbols, quantity a acronyms	57
Attachments	60

List of images

Fig. 2-1: Sketch of the permanent magnet synchronous machines [2]	3
Fig. 2-2: Sketch of the PMASR geometry with description [6].....	4
Fig. 2-3: a) Electromechanical system, b) SRM [7].....	5
Fig. 2-4: Simplified SRAM geometry [7]	7
Fig. 2-5: The equivalent circuit for the d-axis (a) and the q-axis (b) voltages.....	8
Fig. 2-6: The vector diagrams of the PMASR (a) and the SRM (b) machines VD (b)..	9
Fig. 3-1: The Stator replacement described with the conductor distribution [2]	10
Fig. 3-2: The current phase in the electrical degrees [2]	11
Fig. 3-3: Rotor geometry with one flux barrier per pole with references [2].....	12
Fig. 3-4: Magnetic network of PMASR with one flux barrier per pole [2]	13
Fig. 3-5: Magnetic network of PMASR with two flux barriers per pole [2].....	16
Fig. 4-1: FEMAG layout.....	23
Fig. 4-2: Script file example	23
Fig. 4-3: .fsl file example	24
Fig. 4-4: BCH file example.....	24
Fig. 4-5: SRAM1 geometry with the script parameters	25
Fig. 4-6: SRAM2 geometry with the script parameters	25
Fig. 4-7: SRAM3 geometry with the script parameters	26
Fig. 5-1 - Stator slots with script parameters description.....	33
Fig. 5-2 - Stator slots with script parameters description.....	36
Fig. 5-3: M470-50A and M330-35A B-H curves comparison	40
Fig. 6-1 Sketch of the investigated system in Static structural analysis [28]	42
Fig. 6-2 Analysis structure	43
Fig. 6-3 Estimated areas with the highest equivalent stress (Sketch from [28])	43
Fig. 7-1 Torque behavior comparison between FEA and analytical calculation	46
Fig. 8-1 Layout of the test bench and tested motor	48
Fig. 8-2 Magnetic materials [26]	48
Fig. 8-3 Laser cutting influence on material [21].....	49
Fig. 8-4 Relationship between flux density and magnetic intensity behavior	49
Fig. 8-5 Concluded torque reduction	50

List of tables

Table 1 - SMPM motor specifications	27
Table 2 - Ferrite and NdFeB PMASR 12/10 versions with two flux barriers per pole comparison	29
Table 3 - Results of the number of turns and stator current modification on 27/6 combination with two flux barriers per pole	31
Table 4 - Results of the stator PA done on 36/8 combination with two flux barriers per pole	33
Table 5 - Final air gap modification and number of turns/current optimization on 36/8 combination	34
Table 6 - Optimization parameters for flux barriers radiuses.....	36
Table 7 - Results of the Stator PA done on 36/8 combination with two flux barriers per pole	36
Table 8 - Results of the stator PA done on SRAM2 36/8 combination with two flux barriers per pole.....	37
Table 9 - Results of the stator SRAM3 PA done on 36/8 combination.....	38
Table 10 - Comparison of optimized geometries	39
Table 11 - Results of the optimized geometries for M470-50A iron.....	40
Table 12 Recalculated objectives for new copper fill factor and considering the coil overlap.....	41
Table 13 FEA and prototype results comparison	47

1 INTRODUCTION

The first prototype of the synchronous reluctance motor (SRM), the predecessor of permanent magnet assisted synchronous reluctance motor (PMASR), as we know it today was developed by J.K. Kostko in 1923. But even Mr. Kostko thought that the motor would not be extensively used in the future, thanks to its bad efficiency and poor performance characteristics [1]. The academic research done on the SRM, the development of the power converters and the new control algorithms over the years had helped to reduce the SRM drawbacks and made it worthy competitor to the other types of motor. However, some disadvantages of the machine either had not been reduced or could not be reduced, such as the low torque density or low power factor [9].

The PMASR topology, which is the main topic of this thesis, can be considered the enhanced SRM topology. The PMASR geometry is similar to the geometry of SRM, but in addition, PMASR benefits from use of the permanent magnets (PM) inserted inside the rotor. The use of PM is twofold: the first PMs create the electromagnetic torque and the second PMs improve the power factor. Thus, both initial main drawbacks can be reduced by the use of PM.

First, the reason why PMASR geometry was developed will be introduced to the readers. Later, basic PMASR functionality principles will be presented and the motor functionality will be explained by using equations and vector diagrams. After readers become familiar with the machine's principle and behavior, further motor analysis could be done, for example, the analytical model with one and two barriers per pole.

The FEA model scripts written to calculate three different geometry versions will be shown and the motor will be designed to achieve the desired torque. The presented analytical model will be then programmed in Matlab software and calculated results will be used to evaluate the results from FE software.

Chosen FEA model mechanical strength towards the centrifugal force will be investigated in ANSYS software and results will be discussed in this work.

According to the chosen FE model, the prototype will be manufactured and tested. The measured data will be finally compared with the calculated results and possible differences will be investigated and discussed in this thesis.

This thesis should provide good background for the PMASR design process with the possible issues and solutions for problems that might occur.

2 PERMANENT MAGNET ASSISTED SYNCHRONOUS RELUCTANCE MOTOR

Basic principles of investigated motor will be presented. Motor will be described by using derivatives in d - q coordinates and from equations machine equivalent circuits will be created. Motor will be also analyzed and presented in a stable state along with a corresponding vector diagram.

2.1 What is the PMASR

In the family of all electric motors, the permanent magnet assisted synchronous reluctance (PMASR) motor is included in the branch of synchronous motors. The PMASR is more specifically located in the sub-branch of permanent magnet motors with PMs inserted inside the rotor structure (IPM). Beside the IPM motors in the same branch, we can find the surface mounted permanent magnet (SMPM) motors, whose have PM placed on their rotor surface. On Fig. 2-1, sketches of the IPM and the SMPM motors are shown. The gray areas are used for permanent magnets.

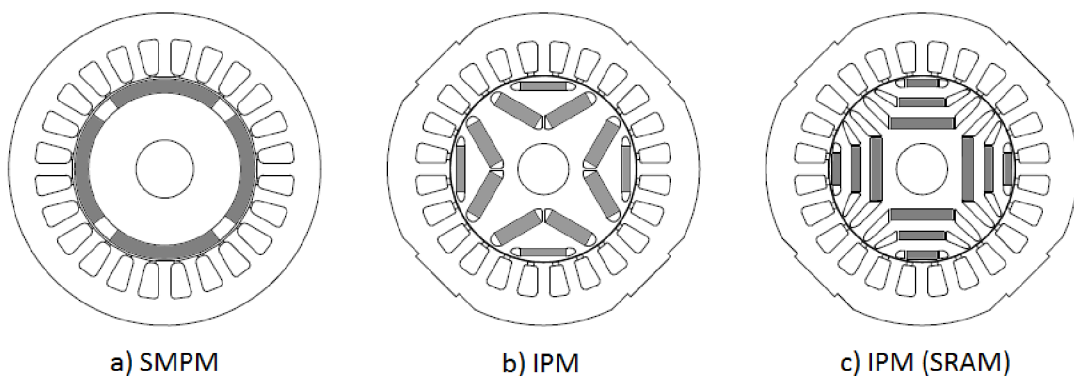


Fig. 2-1: Sketch of the permanent magnet synchronous machines [2]

The PMASR can be used in various applications in many industry branches, from the pump applications [3] through the house applications, such as the washing machines [4], to the ships drives [5]. This implies the need of wide range of rated powers, from hundreds of watts to hundreds of kilowatts and more.

Before the motor will be described with the equations, it is essential to first show and describe the geometry itself. At Fig. 2-2 is the PMASR geometry sketch presented with the description of the rotor geometry. Rotating part „called the rotor” is placed inside the stationary part, „called the stator”. The rotor consists of iron sheets with areas of iron catted out, called the „flux barriers”, where the PMs are inserted. Inside the rotor is the shaft, the part which is rotating along with rotor and delivers the developed torque out of housing.

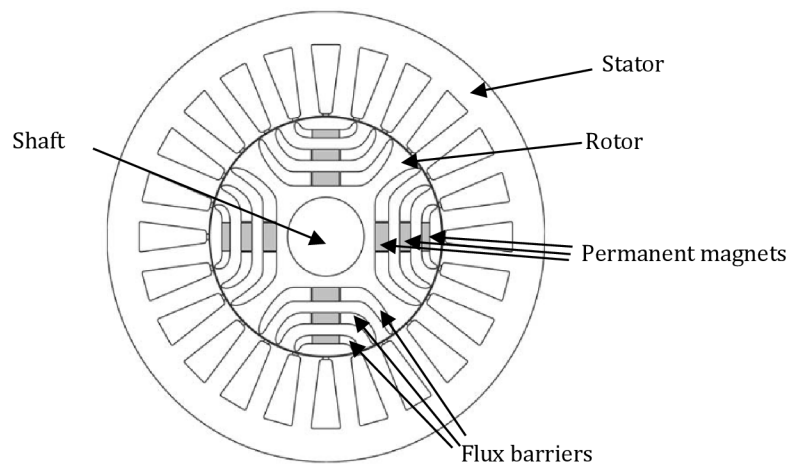


Fig. 2-2: Sketch of the PMASR geometry with description [6]

2.2 Why PMASR?

The SMPM motors, which the PMASR in some cases might replace, have a lot of electric advantages, such as the high power factor and the high torque density. However several issues might occur during their manufacturing process. The first one is that magnets are located on the rotor surface, where the speed, thus the centrifugal force is maximal. Because of the strong force, there is need to use high quality and expensive glue, to fix the magnets on the rotor surface. Besides the high cost of the glue, it has to be applied on the surface in the thin layer equally over the surface, which is difficult to do [12]. The second manufacturing problem is with the magnet eventual displacement, which is listed and described in literature [11].

In the PMASR machine are problems with the magnets (mentioned above) limited, because magnets are inserted in the „pockets” created in the rotor iron. However, as it was said in the abstract, it is possible to use the low-cost ferrite magnets. Concluding this, the PMASR is technologically easier to design and cheaper to manufacture, thus the final cost is lower than the SMPM motor.

2.3 Fundamental equations

Section 2.1 states that the PMASR is synchronous reluctance machine (SRM) with magnets inside the flux barriers. This is the reason why the machine will be described in this chapter firstly as simple electromagnetic system, then as the SRM, and later the PMs will be considered.

Let us first consider the simple electro-mechanical system with the stationary part (stator) and rotating part (rotor) sketched on Fig. 2-3 a). The rotor geometry is designed with the magnetic saliency. The rotor in its one axis is

designed thinner than in the other. The stator has a single coil placed in two slots on both sides of the stator [7].

For sake of simplification, let us consider the relative permeability of the stator and the rotor iron to be $\mu_r \rightarrow \infty$. With this simplification, the magnetic reluctance consists only of the air gap reluctance, because the reluctance of iron results in zero.

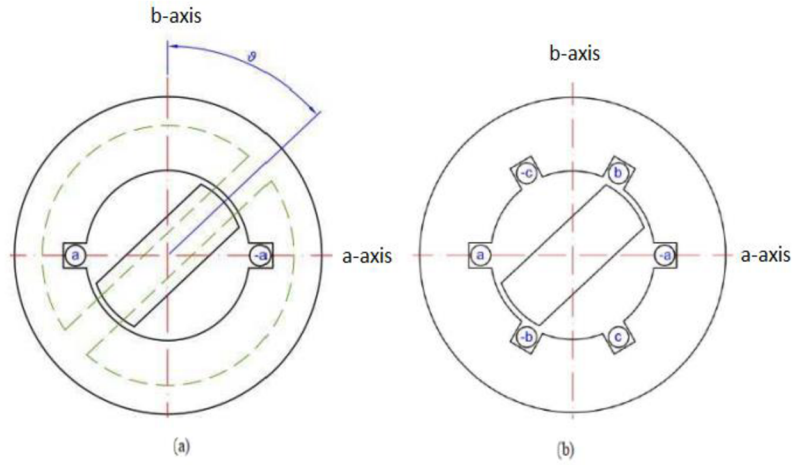


Fig. 2-3: a) Electromechanical system, b) SRM [7]

As it is obvious from the Fig. 2-3 that the magnetic reluctance is different in both axes, because the air gap length is different. This relationship is shown in equation below [8]:

$$R_m = \frac{1}{\mu_0 \cdot \mu_r} \cdot \frac{l}{S} \quad (1.1)$$

Where μ_0 is the permeability of vacuum, l is the air gap length and S is the surface area of the material where the reluctance is calculated. Because the rotor is rotating, therefore the reluctance, measured in coil is varying. It varies between the maximum, when the angle $\vartheta = 0^\circ$ to its minimum, when $\vartheta = 90^\circ$. The two extreme situations imply that the reluctance, and also the inductance are varying with the cosine function. The expression for inductance is in following equation [7]:

$$L_a(\vartheta) = L_{am} \cdot \cos \vartheta \quad (1.2)$$

Where L_{am} is the maximal inductance measured in H and ϑ is the angle between the rotor and the stator coil axis.

In the literature [8], where from the simple energy balance principle and considering the linear magnetic system, the author came up with an equation that can be used in our case for the torque calculation:

$$M_{im} = -\frac{\partial W_m}{\partial \vartheta_m} = \frac{\partial W_{co}}{\partial \vartheta_m} \quad (1.3)$$

Where if the magnetic coenergy W_{co} is substituted by $W_{co} = \frac{i_a^2}{2} \cdot L_a(\vartheta)$, where i_a is the current feeding the stator coil and if L_a is replaced with the formulation 1.2 the final form comes up [6]:

$$M_{im} = -\frac{\partial W_m}{\partial \vartheta_m} = \frac{\partial W_{co}}{\partial \vartheta_m} = \frac{\partial \left(\frac{i_a^2}{2} \cdot L_a(\vartheta) \right)}{\partial \vartheta} = \frac{\partial \left(\frac{i_a^2}{2} \cdot L_{am} \cdot \cos \vartheta \right)}{\partial \vartheta} = -\frac{i_a^2}{2} \cdot L_{am} \cdot \sin \vartheta \quad (1.4)$$

This equation (1.4) finally explains the basic principle of the synchronous reluctance motor. The motor develops the electromagnetic torque, because the inductance varies with the rotating rotor. The designer's goal is to develop a machine with the maximum inductance saliency, which results into the maximum torque created by the motor. To achieve this goal, the rotors are developed with the flux barriers [2].

Even though the electric motor, which was used for explaining the principle, would work, its rotor would not start to rotate. The magnetic field created by stator coil is not rotating, but only pulsating from the one side to the other. Therefore the stator is not designed with one coil and therefore with the single phase winding, but with more coils and the multiple-phase winding instead as shown in Fig. 2-3 b) [7].

The PMs used in the PMASR technology do not suppress the presented SRM principle. Because the PM's relative permeability is almost equal with relative permeability of the air, the inductance remains nearly the same. The PMs develop the new part of the torque. The magnets create the electromagnetic flux that interferes with the flux created by stator, therefore creating a stronger bond between these two parts, thus higher torque. This will be explained and proven by the mathematics in next chapter.

2.4 Mathematic definition of PMASR

The mathematical definition will be provided not in the stationary reference frame, but in the d-q rotating frame instead. If the definition would be performed in the stationary reference frame, it would have to be transformed to the rotating frame at the end. Thus it seems eligible to use the d-q frame from the beginning. In addition, a 2-phase system (d-q frame) is used by AC drives, therefore the model, created later with use of 2-phase system, will be more useful. Simplified model of the SRAM, presented below will serve for the mathematical description. Green area inside the rotating part represents the permanent magnet.

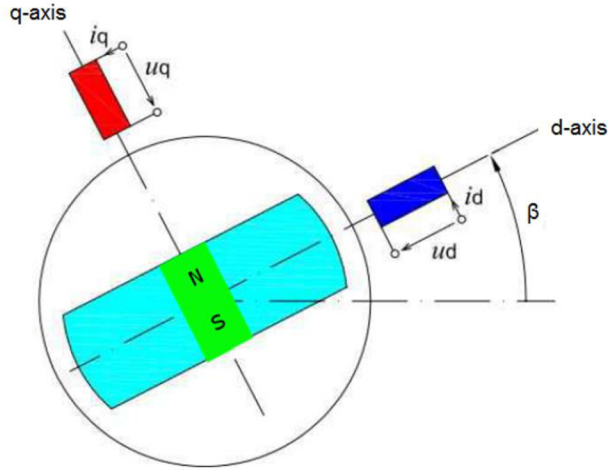


Fig. 2-4: Simplified SRAM geometry [7]

Equations for the stator voltage and the current in the d-q reference frame:

$$u_s = \sqrt{u_d^2 + u_q^2} \quad (1.5)$$

$$i_s = \sqrt{i_d^2 + i_q^2} \quad (1.6)$$

For the voltages in the d and in q axes can be written:

$$u_d = R_d \cdot i_d + \frac{d\psi_d}{dt} - \omega \cdot \psi_q \quad (1.7)$$

$$u_q = R_q \cdot i_q + \frac{d\psi_q}{dt} + \omega \cdot \psi_d \quad (1.8)$$

Where ω is the electrical speed that can be calculated as mechanical speed times number of pole pairs:

$$\omega = p \cdot \omega_{mech} \quad (1.9)$$

For the flux linkages in d and q axes [10]:

$$\psi_d = L_d \cdot i_d \quad (1.10)$$

$$\psi_q = L_q \cdot i_q - \psi_{PM} \quad (1.11)$$

The torque equation presented for example in [8], where on the left side is torque developed by the motor, and on the right side is acceleration and the load torque, can be in the d-q frame written as:

$$\frac{3}{2} \cdot p \cdot (\psi_d \cdot i_q - \psi_q \cdot i_d) = \frac{J}{p} \cdot \frac{d\omega}{dt} + m_{mech} \quad (1.12)$$

Substituting the flux linkages in by expressions (1.10) and (1.11) and after few modifications:

$$\frac{3}{2} \cdot p \cdot [\psi_{PM} \cdot i_d + (L_d - L_q) \cdot i_d \cdot i_q] = \frac{J}{p} \cdot \frac{d\omega}{dt} + m_{mech} \quad (1.13)$$

In equation (1.13) is the mathematical proof, that the PM flux creates the magnetic torque, as noted in chapter 2.

The equivalent circuits with the equations created from the combination of equations (1.7) with the (1.11) and the (1.8) with the (1.10) are presented below.

$$u_d = R_d \cdot i_d + \frac{d\psi_d}{dt} - \omega \cdot L_q \cdot i_q + \omega \cdot \psi_{PM} \quad (1.14)$$

$$u_q = R_q \cdot i_q + \frac{d\psi_q}{dt} + \omega \cdot L_d \cdot i_d \quad (1.15)$$

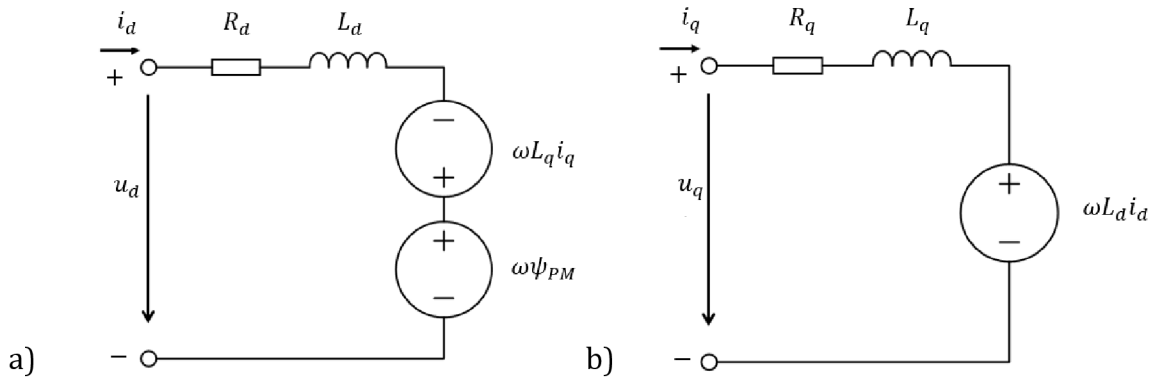


Fig. 2-5: The equivalent circuit for the d-axis (a) and the q-axis (b) voltages

2.5 PMASR in stable state

The stable state means that all the voltages, currents, and flux linkages are constants. All transient values are replaced in the equations with their magnitudes, thus the derivatives are equal to zero. For the vector diagram the voltages, the currents and the flux linkages will be written in complex forms with the d-axis values considered as real and the q-axis values considered as imaginal. The equations transform into:

$$U_s = U_d + jU_q \quad (1.16)$$

$$I_s = I_d + jI_q \quad (1.17)$$

$$\psi_{sm} = \psi_{dm} + j\psi_{qm} \quad (1.18)$$

$$U_d = R_d \cdot I_d - \omega \cdot \psi_{qm} \quad (1.19)$$

$$U_q = R_q \cdot I_q + \omega \cdot \psi_{dm} \quad (1.20)$$

$$\psi_{dm} = L_d \cdot I_d \quad (1.21)$$

$$\psi_{qm} = L_q \cdot I_q - \psi_{PM,m} \quad (1.22)$$

Replacing the flux linkages in (1.19) and (1.20) with (1.21) and (1.22), the voltages in the d and the q axes become:

$$U_d = R_d \cdot I_d - \omega \cdot L_q \cdot I_q + \omega \cdot \psi_{PM,m} \quad (1.23)$$

$$U_q = R_q \cdot I_q + \omega \cdot L_d \cdot I_d \quad (1.24)$$

With the use (1.23) and (1.24), the stator voltage in (1.16) can be expressed as:

$$U_s = U_d + jU_q = R_d \cdot I_d - \omega \cdot L_q \cdot I_q + \omega \cdot \psi_{PM,m} + j(R_q \cdot I_q + \omega \cdot L_d \cdot I_d) \quad (1.25)$$

After some manipulations:

$$U_s = R_d \cdot I_d - \omega \cdot L_q \cdot I_q + \omega \cdot \psi_{PM,m} + j \cdot R_q \cdot I_q + j \cdot \omega \cdot L_d \cdot I_d \quad (1.26)$$

From the equation (1.26) the vector diagram is created and shown with the PMASR vector diagram below:

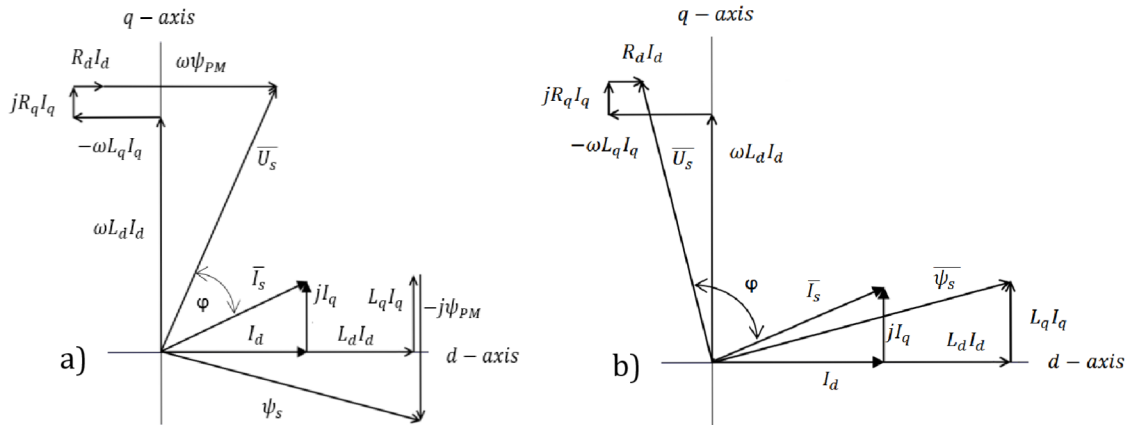


Fig. 2-6: The vector diagrams of the PMASR (a) and the SRM (b) machines VD (b)

3 ANALYTICAL MODEL OF PMASR

In this chapter, an analytical model will be created. The analytical model will be at first created for one flux barrier per pole and then extended to two flux barriers per pole. With the created analytical model will be possible to calculate air gap flux-density and electromagnetic torque.

3.1 Introduction

At first, the reluctance network in the analytical model is presented, then investigated, and then simplified by the laws similar to ones commonly used in the electric circuits [2].

The analytic model of the anisotropic machine, such as the PMASR, is presented in the literature [2], [9]. Firstly the geometry with one flux barrier per pole will be investigated and then the model will be extended to two flux barriers per pole. The purpose of the analytical model is to calculate the electromagnetic torque and evaluate the FEA results.

3.2 Stator analytical model

Stator slots in the analytical model are replaced with a conductive sheet placed on stator inner surface. The “conductor distribution” in conductive sheet is taken into account. Thus the current density is not linear [2]. Considered stator in comparison with original stator is shown in picture below.

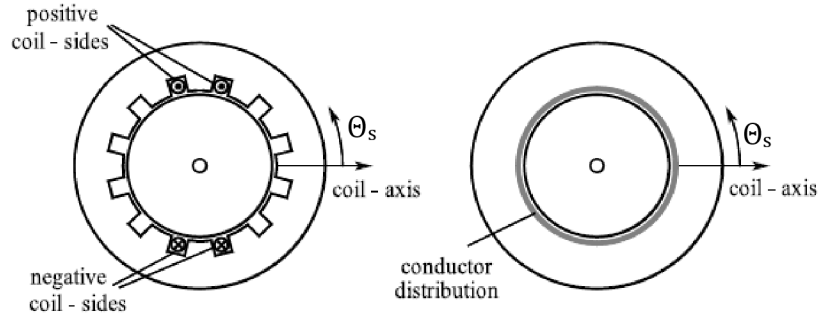


Fig. 3-1: The Stator replacement described with the conductor distribution [2]

3.2.1 Electric loading

Because the conductor distribution over the conductive sheet is non-linear, the current density is non-linear as well. The current density is considered when the current is flowing through the stator coils. The linear current distribution described above is called electrical loading and in literature ([2], [9]) is labeled K_s and calculated in the stator reference frame using the equation [9]:

$$K_s(\vartheta_s) = \sum_n \bar{K}_n \cdot \sin(np\vartheta_s - p\vartheta_m - \alpha_i^e) = \sum_n \bar{K}_n \cdot \sin(np\vartheta_s - \omega_{met} - \alpha_i^e) \quad (1.27)$$

Where [2]: n harmonic order [-]
 \bar{K}_n Peak of the electric loading of the n-harmonic [A/m]
 p number of pole pairs [-]
 ϑ_s angle in stator reference frame in mech. degrees [°mech]
 ϑ_m angular position of the rotor in mechanical degrees [°mech]
 α_i^e Angle measured between the current vector and the d-axis in electrical degrees [°el]

α_i^e is explained in the figure below:

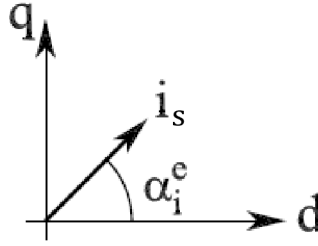


Fig. 3-2: The current phase in the electrical degrees [2]

The electric loading of each harmonic order can be calculated from the equation [9]:

$$\bar{K}_n = \frac{3 \cdot \bar{I} \cdot k_{wn} \cdot N_s}{\pi \cdot D} \cdot \sin\left(\frac{n \cdot \pi}{2}\right) \quad (1.28)$$

Where [9]: k_{wn} winding factor of the n-th harmonic order [-]
 N_s number of conductors per phase [-]
 D inner stator diameter [m]
 \bar{I} Peak value of current in each conductor

3.2.2 Magnetic potential

It is explained in the literature [9] that by integrating of the electric loading, which is spatial vector in distance equal half of the stator inner diameter over the whole conductive sheet, the stator magnetic potential can be calculated, thus:

$$U_{ms}(\vartheta_s) = \int K_s(\vartheta_s) \cdot \frac{D}{2} \cdot d\vartheta_s \quad (1.29)$$

For further calculations it is convenient to express the stator electrical loading in the rotor coordinates. The rotor is rotating at the same speed as the stator magnetic field vector, therefore the difference angle between the stator and the rotor magnetic field is caused only by the mechanical loading i.e. ϑ_m . Thus, the angular coordinate can be computed by [2]:

$$p\vartheta_s = p\vartheta_r + p\vartheta_m = p\vartheta_r + \omega_{me}t \quad (1.30)$$

Where: ω_{me} is electrical speed ($\omega_{mech} = p \cdot \omega_{me}$)

After substituting the electrical loading K_s in (1.29) with the equation (1.27) with considering the rotor coordinates, the stator magnetic potential can be expressed by [2]:

$$U_{ms}(\vartheta_r) = \int \frac{D}{2} \cdot \sum_n \bar{K}_n \cdot \sin(np\vartheta_r + n\omega_{me}t - \omega_{me}t - \alpha_i^e) \cdot d\vartheta_s \quad (1.31)$$

After modifying the equation (1.31) and expressing it only for one pole final form becomes [2]:

$$U_{ms}(\vartheta_r) = -\frac{D}{2p} \cdot \sum_n \frac{\bar{K}_n}{n} \cdot \cos(np\vartheta_r + (n-1)\omega_{me}t - \alpha_i^e) \quad (1.32)$$

3.3 Analytical model of rotor with one flux barrier per pole

Analytical models consider some simplifications e.g. slotless stator in the previous chapter. In the rotor model, the infinite permeability, the constant thickness, and the length of flux barrier is considered. Also, the magnetic bridges at both ends of flux barrier are neglected. To keep the magnetic circuit as simple as possible, the geometry and the magnetic symmetries are considered [2].

3.3.1 Magnetic potential

On the figure below is linearized geometry of the PMASR with the one flux barrier per pole is shown. The angle ϑ_b expresses the half-pole angle of the flux barrier in mechanical degrees.

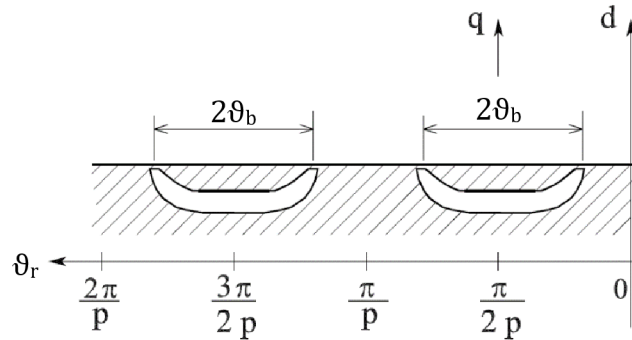


Fig. 3-3: Rotor geometry with one flux barrier per pole with references [2]

In the magnetic circuit, there are reluctances that need to be investigated. First is the reluctance of the air gap and the second is reluctance of the flux barrier itself.

The flux barrier reluctance R_{b1} can be expressed [2]:

$$R_{b1} = \frac{t_b}{\mu_0 \cdot l_{Fe} \cdot l_b} \quad (1.33)$$

Where t_b represents the flux barrier thickness, l_{Fe} is the stack length and l_b is the flux barrier length.

Permanent magnet is in flux barrier and its magnetic flux is calculated [2]:

$$\phi_{PM1} = B_{PM} \cdot l_{Fe} \cdot h_{PM1} = \mu_0 \cdot \mu_r \cdot H_{cPM} \cdot l_{Fe} \cdot h_{PM1} \quad (1.34)$$

In the equation (1.34) B_{PM} represents the residual flux density of the PM buried inside flux barrier, h_{PM1} is the PM height, μ_r is the PM relative permeability and H_{cPM} is the PM coercive force.

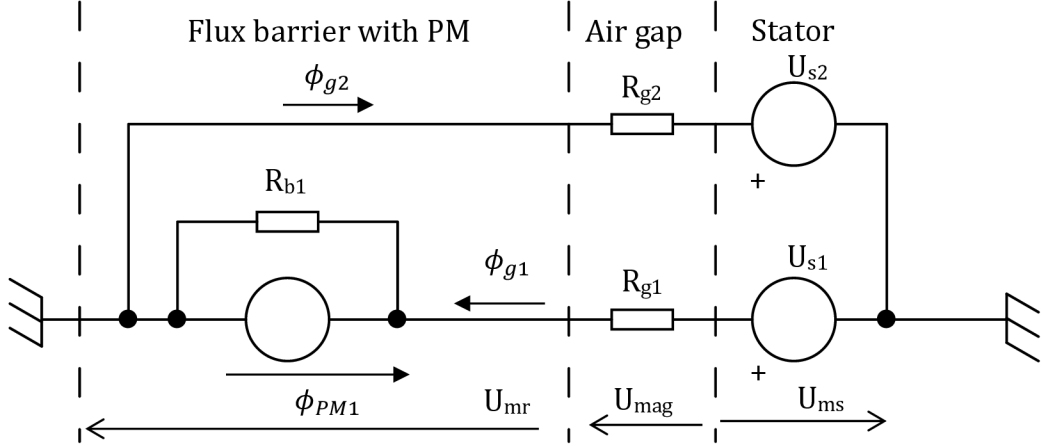


Fig. 3-4: Magnetic network of PMASR with one flux barrier per pole [2]

Applying the second Kirchhoff's law to the magnetic network presented above it results into this equation, which can be modified:

$$U_{mr} + U_{mag} - U_{ms} = 0 \quad (1.35)$$

$$U_{mag} = U_{ms} - U_{mr} \quad (1.36)$$

The expression for the flux density can be written as [8]:

$$B = \mu \cdot H \quad (1.37)$$

Where the magnetic coercivity can be expressed as the magnetic voltage over the length and modified for the network presented in Fig. 3-4 the equation results in [2]:

$$B_g(\vartheta_r) = \mu_0 \cdot \frac{U_{ms} - U_{mr}}{g} \quad (1.38)$$

The rotor magnetic voltage can be calculated [2]:

$$U_{mr} = R_{b1} \cdot (\phi_{PM1} + \phi_{g1}) \quad (1.39)$$

Using the equations (1.33, 1.34) in (1.37) expression results in [2]:

$$U_{mr} = \frac{t_b}{\mu_0 \cdot l_{Fe} \cdot l_b} \cdot \left[\int_{\frac{\pi}{2p} - \vartheta_b}^{\frac{\pi}{2p} + \vartheta_b} \left(B_g(\vartheta_r) \cdot \frac{D}{2} \cdot l_{Fe} \right) d\vartheta_r + \mu_0 \cdot \mu_r \cdot H_{cPM} \cdot l_{Fe} \cdot h_{PM1} \right] \quad (1.40)$$

Replacing the B_g by equation (1.38):

$$U_{mr} = \frac{t_b}{\mu_0 \cdot l_{Fe} \cdot l_b} \cdot \left[\int_{\frac{\pi}{2p} - \vartheta_b}^{\frac{\pi}{2p} + \vartheta_b} \left(\mu_0 \cdot \frac{U_{ms} - U_{mr}}{g} \cdot l_{Fe} \cdot \frac{D}{2} \right) d\vartheta_r + \mu_0 \cdot \mu_r \cdot H_{cPM} \cdot l_{Fe} \cdot h_{PM1} \right] \quad (1.41)$$

It is mentioned in the literature [2], that the rotor magnetic potential is constant over the rotor “island”, which is bordered by the flux barrier and the air gap and null elsewhere. By using this fact and using some manipulations the expression becomes:

$$U_{mr} = \frac{D}{2g} \cdot \frac{t_b}{l_b} \cdot \left(\int_{\frac{\pi}{2p} - \vartheta_b}^{\frac{\pi}{2p} + \vartheta_b} U_{ms}(\vartheta_r) d\vartheta_r - 2 \cdot \vartheta_b \cdot U_{mr} + \frac{2g}{D} \mu_r \cdot H_{cPM} \cdot h_{PM1} \right) \quad (1.42)$$

Taking out the constant rotor magnetic potential from the brackets and moving it on the left side 1.42 changes into [2]:

$$U_{mr} \cdot \left(1 + \frac{D}{2g} \cdot \frac{t_b}{l_b} \cdot 2\vartheta_b \right) = \frac{D}{2g} \cdot \frac{t_b}{l_b} \cdot \left(\int_{\frac{\pi}{2p} - \vartheta_b}^{\frac{\pi}{2p} + \vartheta_b} U_{ms}(\vartheta_r) d\vartheta_r + \frac{2g}{D} \mu_r \cdot H_{cPM} \cdot h_{PM1} \right) \quad (1.43)$$

From the expression in brackets on the left side and expression before the brackets, coefficient can be defined [2]:

$$a = \frac{\frac{D}{2g} \cdot \frac{t_b}{l_b}}{\left(1 + \frac{D}{2g} \cdot \frac{t_b}{l_b} \cdot 2\vartheta_b \right)} \quad (1.44)$$

This constant can be calculated only from the rotor geometry parameters.

The equation thus becomes [2]:

$$U_{mr} = a \cdot \int_{\frac{\pi}{2p} - \vartheta_b}^{\frac{\pi}{2p} + \vartheta_b} U_{ms}(\vartheta_r) d\vartheta_r + a \cdot \frac{2g}{D} \mu_r \cdot H_{cPM} \cdot h_{PM1} \quad (1.45)$$

Using the equation (1.32) [2]:

$$U_{mr} = a \cdot \sum_n \int_{\frac{\pi}{2p} - \vartheta_b}^{\frac{\pi}{2p} + \vartheta_b} -\frac{\bar{K}_n}{n} \cdot \frac{D}{2p} \cdot \cos(np\vartheta_r + (n-1)\omega_{me}t - \alpha_i^e) d\vartheta_r + a \cdot \frac{2g}{D} \mu_r \cdot H_{cPM} \cdot h_{PM1} \quad (1.46)$$

$$U_{mr} = a \cdot \sum_n -\frac{\bar{K}_n}{n} \cdot \frac{D}{2p} \cdot \frac{1}{np} [\sin(np\vartheta_r + (n-1)\omega_{me}t - \alpha_i^e)]_{\frac{\pi}{2p} - \vartheta_b}^{\frac{\pi}{2p} + \vartheta_b} + a \cdot \frac{2g}{D} \mu_r \cdot H_{cPM} \cdot h_{PM1} \quad (1.47)$$

Both parts of the right side can be modified, the second part [2]:

$$a \cdot \frac{2g}{D} \mu_r \cdot H_{cPM} \cdot h_{PM1} = \frac{\frac{D}{2g} \cdot \frac{t_b}{l_b}}{\left(1 + \frac{D}{2g} \cdot \frac{t_b}{l_b} \cdot 2\vartheta_b \right)} \cdot \frac{2g}{D} \cdot \frac{\mu_0}{\mu_r} \cdot \frac{l_{Fe}}{l_{Fe}} \cdot \mu_r \cdot H_{cPM} \cdot h_{PM1} \quad (1.48)$$

$$= \frac{1}{\left(1 + \frac{D}{2g} \cdot \frac{t_b}{l_b} \cdot 2\vartheta_b \right)} \cdot \frac{t_b}{\mu_0 \cdot l_{Fe} \cdot l_b} \cdot \mu_0 \cdot \mu_r \cdot H_{cPM} \cdot h_{PM1} = b \cdot R_{b1} \cdot \phi_{PM1} = k_{PM1} \quad (1.49)$$

Where the k_{PM1} signifies the contribution of the PM [2] and new coefficient is defined:

$$b = \frac{1}{\left(1 + \frac{D}{2g} \cdot \frac{t_b}{l_b} \cdot 2\vartheta_b \right)} \quad (1.50)$$

The first part of the equation can be simplified by the using trigonometric identities and after few modifications results in [2]:

$$a \cdot \sum_n -\frac{\bar{K}_n}{n} \cdot \frac{D}{2p} \cdot \frac{1}{np} [\sin(np\vartheta_r + (n-1)\omega_{me}t - \alpha_i^e)]^{\frac{\pi}{2p} + \vartheta_b} = \quad (1.51)$$

$$a \cdot \sum_n -\frac{\bar{K}_n}{n} \cdot \frac{D}{2p} \cdot \frac{1}{np} \cdot \cos\left(\frac{n\pi}{2} + (n-1)\omega_{me}t - \alpha_i^e\right) \cdot \sin(np\vartheta_b) \quad (1.52)$$

For the sake of further easier orientation, the new coefficient for the expression in brackets is set:

$$\lambda_n = \frac{n\pi}{2} + (n-1)\omega_{me}t - \alpha_i^e \quad (1.53)$$

Finally the original equation (1.47) gets into form:

$$U_{mr} = -a \cdot D \cdot \sum_n \frac{\bar{K}_n}{(np)^2} \cdot \cos \lambda_n \cdot \sin(np\vartheta_b) + k_{PM1} \quad (1.54)$$

3.3.2 Magnetic torque computation

The magnetic torque can be calculated by the integrating Lorentz force over the air gap [2]:

$$M_{ag} = \frac{D}{2} \cdot \int_0^{2\pi} B_g(\vartheta_r) \cdot K_s(\vartheta_r) \cdot \frac{D \cdot l_{Fe}}{2} d\vartheta_r \quad (1.55)$$

$$M_{ag} = \frac{D}{2} \cdot \int_0^{2\pi} \mu_0 \cdot \frac{U_{ms} - U_{mr}}{g} \cdot K_s(\vartheta_r) \cdot \frac{D \cdot l_{Fe}}{2} d\vartheta_r \quad (1.56)$$

$$M_{ag} = \frac{\mu_0 \cdot D^2 \cdot l_{Fe}}{4 \cdot g} \cdot \left[\int_0^{2\pi} U_{ms}(\vartheta_r) \cdot K_s(\vartheta_r) d\vartheta_r - \int_0^{2\pi} U_{mr}(\vartheta_r) \cdot K_s(\vartheta_r) d\vartheta_r \right] \quad (1.57)$$

The first integral is equal to zero, because the U_{ms} and K_s are perpendicular functions, therefore only the second integral remains in torque calculation [2]:

$$M_{ag} = -\frac{\mu_0 \cdot D^2 \cdot l_{Fe}}{4 \cdot g} \cdot \int_0^{2\pi} U_{mr}(\vartheta_r) \cdot K_s(\vartheta_r) d\vartheta_r \quad (1.58)$$

The integral is limited in interval from 0 to 2π , but the magnetic voltage is different from zero in intervals from $\pi/2 - \vartheta_b$ to $\pi/2 + \vartheta_b$ and $3\pi/2 - \vartheta_b$ to $3\pi/2 + \vartheta_b$. It is assumed that the flux barriers are identical, thus using the symmetries, torque developed by one flux barrier can be calculated and multiplied by the number of poles. Hence the torque computation results in [2]:

$$M_{ag} = -\frac{\mu_0 \cdot D^2 \cdot l_{Fe}}{4 \cdot g} \cdot U_{mr} \cdot 2p \int_{\frac{\pi}{2p} - \vartheta_b}^{\frac{\pi}{2p} + \vartheta_b} K_s(\vartheta_r) d\vartheta_r \quad (1.59)$$

By substituting the relationships (1.54) and (1.27) and by defining the new constant torque calculation results in [2]:

$$M_{ag} = -a \cdot k_T \sum_n \frac{\bar{K}_n}{(np)^2} \cdot D \cdot \cos \lambda_n \cdot \sin(np\vartheta_b) \cdot \sum_m \frac{\bar{K}_m}{m} \cdot \sin \lambda_m \cdot \sin(mp\vartheta_b) - k_{PM1} \cdot k_T \sum_m \frac{\bar{K}_m}{m} \cdot \sin \lambda_m \cdot \sin(mp\vartheta_b) \quad (1.60)$$

The defined torque constant is [2]:

$$k_T = \frac{\mu_0 \cdot D^2 \cdot l_{Fe}}{g} \quad (1.61)$$

Let us note, that the torque equation (1.60) has two components, the first one represents the torque caused by the rotor anisotropy and the second one refers to the torque developed by PM flux [2].

3.4 Analytical model of rotor with two flux barriers per pole

The magnetic network presented in chapter 3.3 will be extended to the two flux barriers per pole and the electromagnetic torque will be derived again.

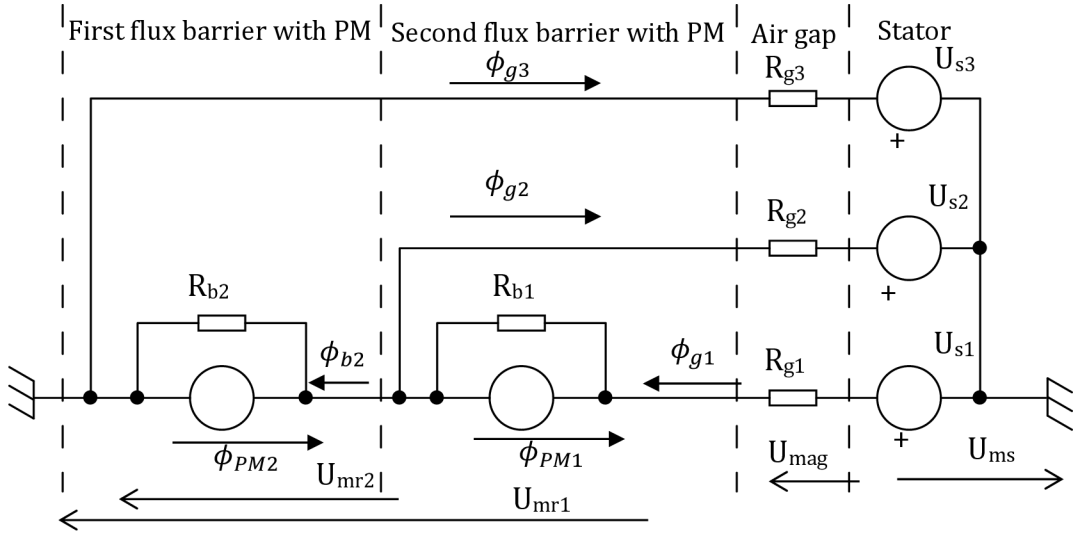


Fig. 3-5: Magnetic network of PMASR with two flux barriers per pole [2]

Both magnetic fluxes developed due the PMs buried in flux barriers can be calculated similar to the equation (1.34), thus:

$$\phi_{PM1} = B_{PM} \cdot l_{Fe} \cdot h_{PM1} = \mu_0 \cdot \mu_r \cdot H_{cPM} \cdot l_{Fe} \cdot h_{PM1} \quad (1.62)$$

$$\phi_{PM2} = B_{PM} \cdot l_{Fe} \cdot h_{PM2} = \mu_0 \cdot \mu_r \cdot H_{cPM} \cdot l_{Fe} \cdot h_{PM2} \quad (1.63)$$

Where:

h_{PM1} , h_{PM2} PM height of outer (1) and inner (2) flux barrier respectively.

In the designing process, it is intended to use only one type of the PM in both flux barriers, therefore both equations differ only in the PM heights. Remaining variables are listed and noted below the equation (1.34).

3.4.1 Rotor magnetic potential

Both variables that will be used in this subchapter (the electric loading and the stator magnetic potential) are defined in previous chapters in the equations (1.27) and (1.32). In this subchapter will be dealt with the total rotor magnetic potential [2].

3.4.1.1 Top flux barrier magnetic voltage

For magnetic voltage on the top flux barrier, the equation can be written [2]:

$$U_{mr1} = R_{b1} \cdot (\phi_{g1} + \phi_{PM1}) + U_{mr2} \quad (1.64)$$

$$U_{mr1} = R_{b1} \cdot \int_{\frac{\pi}{2p} - \vartheta_{b1}}^{\frac{\pi}{2p} + \vartheta_{b1}} \left(B_g(\vartheta_r) \cdot \frac{D}{2} \cdot l_{Fe} \right) d\vartheta_r + R_{b1} \cdot \phi_{PM1} + U_{mr2} \quad (1.65)$$

$$U_{mr1} = R_{b1} \cdot \int_{\frac{\pi}{2p} - \vartheta_{b1}}^{\frac{\pi}{2p} + \vartheta_{b1}} \left(\mu_0 \cdot \frac{U_{ms}(\vartheta_r) - U_{mr1}(\vartheta_r)}{g} \cdot \frac{D}{2} \cdot l_{Fe} \right) d\vartheta_r + R_{b1} \cdot \phi_{PM1} + U_{mr2} \quad (1.66)$$

$$U_{mr1} = \frac{t_{b1}}{\mu_0 \cdot l_{Fe} \cdot l_{b1}} \cdot \int_{\frac{\pi}{2p} - \vartheta_{b1}}^{\frac{\pi}{2p} + \vartheta_{b1}} \left(\mu_0 \cdot \frac{U_{ms}(\vartheta_r) - U_{mr1}(\vartheta_r)}{g} \cdot \frac{D}{2} \cdot l_{Fe} \right) d\vartheta_r + R_{b1} \cdot \phi_{PM1} + U_{mr2} \quad (1.67)$$

$$U_{mr1} = \frac{D \cdot t_{b1}}{2 \cdot g \cdot l_{b1}} \cdot \left[\int_{\frac{\pi}{2p} - \vartheta_{b1}}^{\frac{\pi}{2p} + \vartheta_{b1}} U_{ms}(\vartheta_r) d\vartheta_r - \int_{\frac{\pi}{2p} - \vartheta_{b1}}^{\frac{\pi}{2p} + \vartheta_{b1}} U_{mr1}(\vartheta_r) d\vartheta_r \right] + R_{b1} \cdot \phi_{PM1} + U_{mr2} \quad (1.68)$$

$$U_{mr1} = \frac{D \cdot t_{b1}}{2 \cdot g \cdot l_{b1}} \cdot \left[\int_{\frac{\pi}{2p} - \vartheta_{b1}}^{\frac{\pi}{2p} + \vartheta_{b1}} U_{ms}(\vartheta_r) d\vartheta_r - 2 \cdot \vartheta_{b1} \cdot U_{mr1} \right] + R_{b1} \cdot \phi_{PM1} + U_{mr2} \quad (1.69)$$

$$U_{mr1} \cdot \left(1 + \frac{D \cdot t_{b1}}{2 \cdot g \cdot l_{b1}} \cdot 2\vartheta_{b1} \right) = \frac{D \cdot t_{b1}}{2 \cdot g \cdot l_{b1}} \cdot \int_{\frac{\pi}{2p} - \vartheta_{b1}}^{\frac{\pi}{2p} + \vartheta_{b1}} U_{ms}(\vartheta_r) d\vartheta_r + R_{b1} \cdot \phi_{PM1} + U_{mr2} \quad (1.70)$$

$$U_{mr1} = \frac{\frac{D \cdot t_{b1}}{2 \cdot g \cdot l_{b1}}}{\left(1 + \frac{D \cdot t_{b1}}{2 \cdot g \cdot l_{b1}} \cdot 2\vartheta_{b1} \right)} \cdot \int_{\frac{\pi}{2p} - \vartheta_{b1}}^{\frac{\pi}{2p} + \vartheta_{b1}} U_{ms}(\vartheta_r) d\vartheta_r + \frac{1}{\left(1 + \frac{D \cdot t_{b1}}{2 \cdot g \cdot l_{b1}} \cdot 2\vartheta_{b1} \right)} \cdot R_{b1} \cdot \phi_{PM1} + \frac{1}{\left(1 + \frac{D \cdot t_{b1}}{2 \cdot g \cdot l_{b1}} \cdot 2\vartheta_{b1} \right)} \cdot U_{mr2} \quad (1.71)$$

Where the fractions can be replaced by slightly modified defined coefficients a in (1.44) and b in (1.50) and then the second part modified ($\vartheta_b \rightarrow \vartheta_{b1}$) as shown in eq. (1.48, 1.49), thus the first flux barrier magnetic voltage can be calculated [2]:

$$U_{mr1} = a \cdot \int_{\frac{\pi}{2p} - \vartheta_{b1}}^{\frac{\pi}{2p} + \vartheta_{b1}} U_{ms}(\vartheta_r) d\vartheta_r + k_{PM1} + b \cdot U_{mr2} \quad (1.72)$$

3.4.1.2 Bottom flux barrier magnetic voltage

Magnetic voltage on bottom flux barrier can be calculated [2]:

$$U_{mr2} = R_{b2} \cdot (\phi_{b2} + \phi_{PM2}) \quad (1.73)$$

$$U_{mr2} = R_{b2} \cdot \left[\frac{U_{mr1} - U_{mr2}}{R_{b1}} + \int_{\frac{\pi}{2p} - \vartheta_{b2}}^{\frac{\pi}{2p} - \vartheta_{b1}} B_g(\vartheta_r) \frac{D}{2} l_{Fe} d\vartheta_r + \int_{\frac{\pi}{2p} + \vartheta_{b1}}^{\frac{\pi}{2p} + \vartheta_{b2}} B_g(\vartheta_r) \frac{D}{2} l_{Fe} d\vartheta_r + R_{b2} \cdot \phi_{PM2} \right] \quad (1.74)$$

$$U_{mr2} = R_{b2} \cdot \left[\frac{U_{mr1}(\vartheta_r) - U_{mr2}(\vartheta_r)}{R_{b1}} - \phi_{PM1} + \int_{\frac{\pi}{2p} - \vartheta_{b2}}^{\frac{\pi}{2p} - \vartheta_{b1}} B_g(\vartheta_r) \frac{D}{2} l_{Fe} d\vartheta_r + \int_{\frac{\pi}{2p} + \vartheta_{b1}}^{\frac{\pi}{2p} + \vartheta_{b2}} B_g(\vartheta_r) \frac{D}{2} l_{Fe} d\vartheta_r + \phi_{PM2} \right] \quad (1.75)$$

$$U_{mr2} = R_{b2} \cdot \left[\frac{U_{mr1}(\vartheta_r) - U_{mr2}(\vartheta_r)}{R_{b1}} - \phi_{PM1} + \int_{\frac{\pi}{2p} - \vartheta_{b2}}^{\frac{\pi}{2p} - \vartheta_{b1}} \mu_0 \frac{U_{ms}(\vartheta_r) - U_{mr2}(\vartheta_r) D}{g} \frac{D}{2} l_{Fe} d\vartheta_r + \int_{\frac{\pi}{2p} + \vartheta_{b1}}^{\frac{\pi}{2p} + \vartheta_{b2}} \mu_0 \frac{U_{ms}(\vartheta_r) - U_{mr2}(\vartheta_r) D}{g} \frac{D}{2} l_{Fe} d\vartheta_r \right] + R_{b2} \cdot \phi_{PM2} \quad (1.76)$$

$$U_{mr2} = R_{b2} \cdot \left[\frac{U_{mr1}(\vartheta_r) - U_{mr2}(\vartheta_r)}{\frac{t_{b1}}{\mu_0 l_{Fe} l_{b1}}} + \int_{\frac{\pi}{2p} - \vartheta_{b2}}^{\frac{\pi}{2p} - \vartheta_{b1}} \mu_0 \frac{U_{ms}(\vartheta_r) - U_{mr2}(\vartheta_r) D}{g} \frac{D}{2} l_{Fe} d\vartheta_r + \int_{\frac{\pi}{2p} + \vartheta_{b1}}^{\frac{\pi}{2p} + \vartheta_{b2}} \mu_0 \frac{U_{ms}(\vartheta_r) - U_{mr2}(\vartheta_r) D}{g} \frac{D}{2} l_{Fe} d\vartheta_r \right] + R_{b2} \cdot (\phi_{PM2} - \phi_{PM1}) \quad (1.77)$$

$$U_{mr2} = \frac{t_{b2}}{\mu_0 l_{Fe} l_{b2}} \cdot \left[(U_{mr1}(\vartheta_r) - U_{mr2}(\vartheta_r)) \frac{\mu_0 \cdot l_{Fe} \cdot l_{b1}}{t_{b1}} + \int_{\frac{\pi}{2p} - \vartheta_{b2}}^{\frac{\pi}{2p} - \vartheta_{b1}} \frac{\mu_0 D l_{Fe}}{2g} (U_{ms}(\vartheta_r) - U_{mr2}(\vartheta_r)) d\vartheta_r + \int_{\frac{\pi}{2p} + \vartheta_{b1}}^{\frac{\pi}{2p} + \vartheta_{b2}} \frac{\mu_0 D l_{Fe}}{2g} (U_{ms}(\vartheta_r) - U_{mr2}(\vartheta_r)) d\vartheta_r \right] + R_{b2} \cdot (\phi_{PM2} - \phi_{PM1}) \quad (1.78)$$

$$U_{mr2} = \frac{t_{b2}}{l_{b2}} \cdot \left[(U_{mr1}(\vartheta_r) - U_{mr2}(\vartheta_r)) \frac{l_{b1}}{t_{b1}} + \frac{D}{2g} \int_{\frac{\pi}{2p} - \vartheta_{b2}}^{\frac{\pi}{2p} - \vartheta_{b1}} U_{ms}(\vartheta_r) d\vartheta_r - \frac{D}{2g} \int_{\frac{\pi}{2p} - \vartheta_{b2}}^{\frac{\pi}{2p} - \vartheta_{b1}} U_{mr2}(\vartheta_r) d\vartheta_r + \frac{D}{2g} \int_{\frac{\pi}{2p} + \vartheta_{b1}}^{\frac{\pi}{2p} + \vartheta_{b2}} U_{ms}(\vartheta_r) d\vartheta_r - \frac{D}{2g} \int_{\frac{\pi}{2p} + \vartheta_{b1}}^{\frac{\pi}{2p} + \vartheta_{b2}} U_{mr2}(\vartheta_r) d\vartheta_r \right] + R_{b2} \cdot (\phi_{PM2} - \phi_{PM1}) \quad (1.79)$$

Substituting the first flux barrier magnetic voltage by the expression 1.72 [2]:

$$U_{mr2} = \frac{t_{b2}}{l_{b2}} \cdot \left[\left(a \int_{\frac{\pi}{2p} - \vartheta_{b1}}^{\frac{\pi}{2p} + \vartheta_{b1}} U_{ms}(\vartheta_r) d\vartheta_r + k_{PM1} + b U_{mr2} - U_{mr2}(\vartheta_r) \right) \frac{l_{b1}}{t_{b1}} + \frac{D}{2g} \int_{\frac{\pi}{2p} - \vartheta_{b2}}^{\frac{\pi}{2p} - \vartheta_{b1}} U_{ms}(\vartheta_r) d\vartheta_r - \frac{D}{2g} \int_{\frac{\pi}{2p} - \vartheta_{b2}}^{\frac{\pi}{2p} - \vartheta_{b1}} U_{mr2}(\vartheta_r) d\vartheta_r + \frac{D}{2g} \int_{\frac{\pi}{2p} + \vartheta_{b1}}^{\frac{\pi}{2p} + \vartheta_{b2}} U_{ms}(\vartheta_r) d\vartheta_r - \frac{D}{2g} \int_{\frac{\pi}{2p} + \vartheta_{b1}}^{\frac{\pi}{2p} + \vartheta_{b2}} U_{mr2}(\vartheta_r) d\vartheta_r \right] + R_{b2} (\phi_{PM2} - \phi_{PM1}) \quad (1.80)$$

After few modifications and assuming, that the rotor magnetic voltage U_{mr2} over the second magnetic “island” is same and constant on both sides, the equation results in [2]:

$$\begin{aligned}
U_{mr2} & \left[1 - \frac{l_{b1}}{t_{b1}}(b-1) + \frac{D}{g}(\vartheta_{b2} - \vartheta_{b1}) \right] \\
& = a \frac{t_{b2} l_{b1}}{l_{b2} t_{b1}} \int_{\frac{\pi}{2p} - \vartheta_{b1}}^{\frac{\pi}{2p} + \vartheta_{b1}} U_{ms}(\vartheta_r) d\vartheta_r + \frac{D}{2g} \left[\int_{\frac{\pi}{2p} - \vartheta_{b2}}^{\frac{\pi}{2p} - \vartheta_{b1}} U_{ms}(\vartheta_r) d\vartheta_r + \int_{\frac{\pi}{2p} + \vartheta_{b1}}^{\frac{\pi}{2p} + \vartheta_{b2}} U_{ms}(\vartheta_r) d\vartheta_r \right] \\
& + \frac{t_{b2} l_{b1}}{l_{b2} t_{b1}} k_{PM1} + R_{b2} \cdot (\phi_{PM2} - \phi_{PM1})
\end{aligned} \tag{1.81}$$

To simplify the equation, coefficients c , d and k_{PM2} are defined [2]:

$$c = \frac{a \cdot \frac{t_{b2}}{l_{b2}} \cdot \frac{l_{b1}}{t_{b1}}}{1 - \frac{l_{b1}}{t_{b1}}(b-1) + \frac{D}{g}(\vartheta_{b2} - \vartheta_{b1})} \tag{1.82}$$

$$d = \frac{\frac{D}{2g} \cdot \frac{t_{b2}}{l_{b2}}}{1 - \frac{l_{b1}}{t_{b1}} \cdot \frac{t_{b2}}{l_{b2}} \cdot (b-1) + \frac{D}{g} \cdot \frac{t_{b2}}{l_{b2}} \cdot (\vartheta_{b2} - \vartheta_{b1})} \tag{1.83}$$

$$k_{PM2} = \frac{\frac{t_{b2} l_{b1}}{l_{b2} t_{b1}} k_{PM1} + R_{b2} \cdot (\phi_{PM2} - \phi_{PM1})}{1 - \frac{l_{b1}}{t_{b1}} \cdot \frac{t_{b2}}{l_{b2}} \cdot (b-1) + \frac{D}{g} \cdot \frac{t_{b2}}{l_{b2}} \cdot (\vartheta_{b2} - \vartheta_{b1})} \tag{1.84}$$

Hence the equation (1.81) becomes [2]:

$$U_{mr2} = c \int_{\frac{\pi}{2p} - \vartheta_{b1}}^{\frac{\pi}{2p} + \vartheta_{b1}} U_{ms}(\vartheta_r) d\vartheta_r + d \left[\int_{\frac{\pi}{2p} - \vartheta_{b2}}^{\frac{\pi}{2p} - \vartheta_{b1}} U_{ms}(\vartheta_r) d\vartheta_r + \int_{\frac{\pi}{2p} + \vartheta_{b1}}^{\frac{\pi}{2p} + \vartheta_{b2}} U_{ms}(\vartheta_r) d\vartheta_r \right] + k_{PM2} \tag{1.85}$$

At this point it is possible to express the magnetic voltage with the electric loading, thus the equation becomes [2]:

$$\begin{aligned}
U_{mr2} & = c \sum_n -\frac{\bar{K}_n}{(np)^2} \cos \lambda_n \sin(np\vartheta_{b1}) \\
& + d \left[\sum_n -\frac{\bar{K}_n}{(np)^2} \cos \lambda_n \sin(np\vartheta_{b2}) + \sum_n \frac{\bar{K}_n}{(np)^2} \cos \lambda_n \sin(np\vartheta_{b1}) \right] + k_{PM2}
\end{aligned} \tag{1.86}$$

$$U_{mr2} = -\sum_n \frac{\bar{K}_n}{(np)^2} D \cos \lambda_n [c \cdot \sin(np\vartheta_{b1}) + d \cdot \sin(np\vartheta_{b2}) - d \cdot \sin(np\vartheta_{b1})] + k_{PM2} \tag{1.87}$$

$$U_{mr2} = -\sum_n \frac{\bar{K}_n}{(np)^2} D \cos \lambda_n [(c-d) \cdot \sin(np\vartheta_{b1}) + d \cdot \sin(np\vartheta_{b2})] + k_{PM2} \tag{1.88}$$

With this equation, we can express also the magnetic voltage of the first flux barrier obtained above in (1.72) [2]:

$$U_{mr1} = a \cdot \int_{\frac{\pi}{2p} - \vartheta_{b1}}^{\frac{\pi}{2p} + \vartheta_{b1}} U_{ms}(\vartheta_r) d\vartheta_r + k_{PM1} + b \cdot U_{mr2} \tag{1.89}$$

$$\begin{aligned}
U_{mr1} & = a \sum_n -\frac{\bar{K}_n}{(np)^2} D \cos \lambda_n \sin(np\vartheta_{b1}) + k_{PM1} \\
& - b \sum_n \frac{\bar{K}_n}{(np)^2} D \cos \lambda_n [(c-d) \cdot \sin(np\vartheta_{b1}) + d \cdot \sin(np\vartheta_{b2})] + b \cdot k_{PM2}
\end{aligned} \tag{1.90}$$

$$\begin{aligned}
U_{mr1} & = -\sum_n \frac{\bar{K}_n}{(np)^2} D \cos \lambda_n [a \sin(np\vartheta_{b1}) + b(c-d) \cdot \sin(np\vartheta_{b1}) + bd \cdot \sin(np\vartheta_{b2})] + k_{PM1} \\
& + bk_{PM2}
\end{aligned} \tag{1.91}$$

It is convenient to replace long expressions in brackets with coefficients, because equation (1.91) and (1.88) will be used in the torque calculation. [2]:

$$\alpha_1 = a \sin(np\vartheta_{b1}) + b(c - d) \cdot \sin(np\vartheta_{b1}) + bd \cdot \sin(np\vartheta_{b2}) \quad (1.92)$$

$$\alpha_2 = (c - d) \cdot \sin(np\vartheta_{b1}) + d \cdot \sin(np\vartheta_{b2}) \quad (1.93)$$

Hence the equations (1.88) and (1.91) results in [2]:

$$U_{mr2} = - \sum_n \frac{\bar{K}_n}{(np)^2} D\alpha_2 \cos \lambda_n + k_{PM2} \quad (1.94)$$

$$U_{mr1} = - \sum_n \frac{\bar{K}_n}{(np)^2} D\alpha_1 \cos \lambda_n + k_{PM1} + bk_{PM2} \quad (1.95)$$

3.4.2 Torque calculation

Similarly to the torque calculation in chapter 3.3.2, can be the electromagnetic torque calculated [2]:

$$M_{ag} = \frac{D}{2} \cdot \int_0^{2\pi} B_g(\vartheta_r) \cdot K_s(\vartheta_r) \cdot \frac{D \cdot I_{Fe}}{2} d\vartheta_r \quad (1.96)$$

$$M_{ag} = \frac{\mu_0 \cdot D^2 \cdot I_{Fe}}{4 \cdot g} \cdot \int_0^{2\pi} -U_{mr}(\vartheta_r) \cdot K_s(\vartheta_r) d\vartheta_r \quad (1.97)$$

Substituting the torque constant from (1.61) and the magnetic rotor voltage [2]:

$$M_{ag} = \frac{k_T}{2} (-2p) \cdot \left[\int_{\frac{\pi}{2p} + \vartheta_{b1}}^{\frac{\pi}{2p} + \vartheta_{b2}} U_{mr2} \cdot K_s(\vartheta_r) d\vartheta_r + \int_{\frac{\pi}{2p} - \vartheta_{b1}}^{\frac{\pi}{2p} + \vartheta_{b1}} U_{mr1} \cdot K_s(\vartheta_r) d\vartheta_r + \int_{\frac{\pi}{2p} - \vartheta_{b2}}^{\frac{\pi}{2p} - \vartheta_{b1}} U_{mr2} \cdot K_s(\vartheta_r) d\vartheta_r \right] \quad (1.98)$$

By using the similar modification technique like in case of the rotor with one flux barrier per pole and by substituting expressions for the magnetic voltages [2]:

$$M_{ag} = \frac{k_T \cdot p}{2} \left[\sum_n \frac{\bar{K}_n}{(np)^2} D\alpha_2 \cos \lambda_n \cdot \sum_m \bar{K}_m \left(\alpha_2 \int_{\frac{\pi}{2p} + \vartheta_{b1}}^{\frac{\pi}{2p} + \vartheta_{b2}} \sin(\lambda_m) d\vartheta_r + \alpha_1 \int_{\frac{\pi}{2p} - \vartheta_{b1}}^{\frac{\pi}{2p} + \vartheta_{b1}} \sin(\lambda_m) d\vartheta_r + \alpha_2 \int_{\frac{\pi}{2p} - \vartheta_{b2}}^{\frac{\pi}{2p} - \vartheta_{b1}} \sin(\lambda_m) d\vartheta_r \right) + \sum_m \bar{K}_m \left(k_{PM2} \int_{\frac{\pi}{2p} + \vartheta_{b1}}^{\frac{\pi}{2p} + \vartheta_{b2}} \sin(\lambda_m) d\vartheta_r + k_{PM1} \int_{\frac{\pi}{2p} - \vartheta_{b1}}^{\frac{\pi}{2p} + \vartheta_{b1}} \sin(\lambda_m) d\vartheta_r + k_{PM2} \int_{\frac{\pi}{2p} - \vartheta_{b2}}^{\frac{\pi}{2p} - \vartheta_{b1}} \sin(\lambda_m) d\vartheta_r \right) \right] \quad (1.99)$$

Where the k_T is defined in (1.61), λ_n in (1.53) and λ_m can be calculated very similarly to (1.53) by [2]:

$$\lambda_m = \frac{m\pi}{2} + (m - 1)\omega_{me}t - \alpha_i^e = [^\circ mech] \quad (1.100)$$

The integrals in (1.99) can be further modified [2]:

$$\int_{\frac{\pi}{2p}-\vartheta_{b1}}^{\frac{\pi}{2p}+\vartheta_{b1}} \sin(\lambda_m) d\vartheta_r = \frac{1}{mp} [\cos(\lambda_m + mp\vartheta_{b1}) - \cos(\lambda_m - mp\vartheta_{b1})] = \frac{2}{mp} \cdot \sin\lambda_m \cdot \sin(mp\vartheta_{b1}) \quad (1.101)$$

$$\int_{\frac{\pi}{2p}+\vartheta_{b1}}^{\frac{\pi}{2p}+\vartheta_{b2}} \sin(\lambda_m) d\vartheta_r = \frac{2}{mp} \cdot \sin\lambda_m \cdot \sin(mp\vartheta_{b1}) \quad (1.102)$$

$$\int_{\frac{\pi}{2p}-\vartheta_{b2}}^{\frac{\pi}{2p}-\vartheta_{b1}} \sin(\lambda_m) d\vartheta_r = -\frac{2}{mp} \cdot \sin\lambda_m \cdot \sin(mp\vartheta_{b2}) \quad (1.103)$$

Thus, the final form of (1.96) becomes [2]:

$$\begin{aligned} M_{ag} = k_T \cdot \sum_n \frac{\bar{K}_n}{(np)^2} D\alpha_2 \cos \lambda_n \left[\alpha_2 \sum_m \frac{\bar{K}_m}{m} \cdot \sin\lambda_m \cdot \sin(mp\vartheta_{b2}) + (\alpha_1 - \alpha_2) \sum_m \frac{\bar{K}_m}{m} \cdot \sin\lambda_m \cdot \sin(mp\vartheta_{b1}) \right] \\ - k_T \left[(k_{PM1} + (b-1)k_{PM2}) \sum_m \frac{\bar{K}_m}{m} \cdot \sin\lambda_m \cdot \sin(mp\vartheta_{b1}) \right. \\ \left. + k_{PM2} \sum_m \frac{\bar{K}_m}{m} \cdot \sin\lambda_m \cdot \sin(mp\vartheta_{b2}) \right] \end{aligned} \quad (1.104)$$

4 FEA MODEL

PMASR models for FEA software will be presented in chapter 4. Some FEM basic information will be given as well. FEA models are created with scripts and are calculated in 2D FEA software named FEMAG. Scripts will not be described detail by detail, but only cursorily. Sets of parameters and theirs influence on geometry will be described hereafter.

4.1 Introduction

For complicated geometries, which the PMASR geometry surely is, the fastest way to design and optimize certain geometry is using the finite element analysis. It is obvious from the third chapter that to obtain the analytical model takes a lot of mathematical modifications. Even though the optimization would be faster after that, there are still few neglects that need to be remembered [13], e.g. not considering the iron saturation, or the constant magnetic voltage over the rotor “island” [2]. The finite element method takes into account all these facts.

4.2 Finite element method

The finite element method is a method based on dividing surface into a known amount of small elements, thus finite element method. In the finite elements are the unknown functions which need to be obtained. The function is approximated by the simple interpolating functions with coefficients. The solution of FEM is found when the coefficients of these functions are obtained. The FEM itself consists of these steps [13]:

1. Partition of the domain: Dividing the domain (surface) into elements.
2. Choice of the interpolating functions: The simple functions with coefficients are chosen.
3. Formulation of the system to resolve the problem: The system of equations, representing the solution either Galerkin's method (differentials) or Rayleigh-Ritz (integrals) method is created.
4. Solution.

For the magnetic field problems, usually 2D analysis is used. The reason is that 3D analysis requires larger processing power and long computation time to solve the problem [13].

4.3 Software

Because the PMASR prototype is designed with and for Baumüller Company, its software will be used. The company uses software called FEMAG. The FEMAG was originally developed from 1982 to 1997 at the Institute for Electrical Machines at the ETH Zurich. The FEMAG has various versions, DC, AC, ME, TH. The DC version

was developed to analyze the static magnetic fields and is used for the motors, transformers, relays, etc. The AC version is used to calculate planar, quasi-stationary magnetic field and the eddy currents. The ME and TH versions were developed for mechanical and thermal calculations. For our calculations the DC version will be used [14]. FEMAG layout is shown on the picture below.

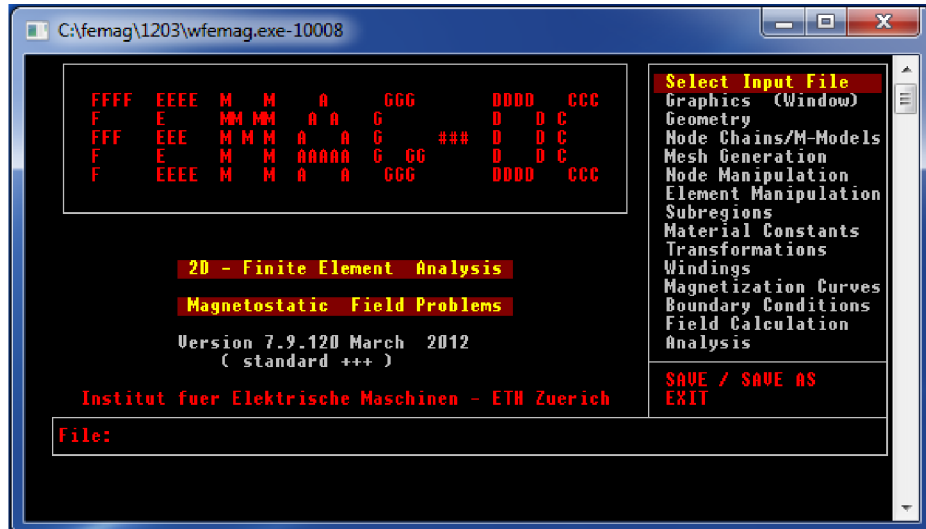


Fig. 4-1: FEMAG layout

The software can be either controlled by the keyboard and mouse and models can be created manually, or as it will be used in this thesis, via script file. The software is very simple, but serves the motor calculating purpose very well.

4.4 Scripts

The scripts are pieces of code that control the program. The script files for the FEMAG are written in the LUA scripting language, which was developed at the University of Rio de Janeiro in Brazil in 1993. The script is written in the classical .txt file. The script file is called from the .fsl file, where all the script parameters and their values are located. Both files are easily editable, for example, in the simple „Notepad” software. The third file is where the FEMAG exports calculation result. The file type is .BCH and can be also opened in „Notepad” software, like the files above. The examples of all three files are shown on the images below:

```

-----
-- Definovani mesh --
-----
create_mesh_se (pd2c(x1_L+0.01, x1_r+phi_ref_r+0.01))
file:write("Mesh created in shaft", "\n")
create_mesh_se (pd2c(x2_L+0.2,x1_r+phi_ref_r+0.2))
file:write("Mesh created in rotor", "\n")

```

Fig. 4-2: Script file example

```

-- CAD - parameter data: SRM2

di_ry = 32 -- [ mm ]
di_sh = 2 -- [ mm ]
poles = 8 -- [ - ]
poles_sim = 2 -- [ - ]

```

Fig. 4-3: .fsl file example

```

[*****]
Machine Data:

Number of phases                :      3
Current Rms value                [A] :      .79
Current loading (RMS)           [kA/m] :     54.62
Current Density (RMS)           [A/mm2] :     6.92
Cu fillfactor                    [%] :     45.00
Therm.Loading A*J (RMS)         [A/cm.mm2] :    3782.20
torque [Nm]                      :      2.25
Force Density                    [kN/m2] :     31.98
Stator-Fe-Losses                 [W] :      3.10
Rotor-Fe-Losses                  [W] :      .00
Magnet-Losses                    [W] :      .15
Cu-Losses                        [W] :      .00
Armature Length                  [mm] :     60.00
Speed                            [1/min] :    1300.00
Mechanical Power                  [kW] :      .31
Efficiency                       :     98.94
[*****]
Calculation time [sec]:
2983
[*****]

```

Fig. 4-4.BCH file example

For the PMASR designing purpose, three scripts were written. Thus three types of geometries are possible to create. All three scripts have their sets of parameters that affect the geometry in a certain way. On pictures below geometries that can be generated with parameters are shown. The scripts will be referred as the SRAM1, the SRAM2 and the SRAM3.

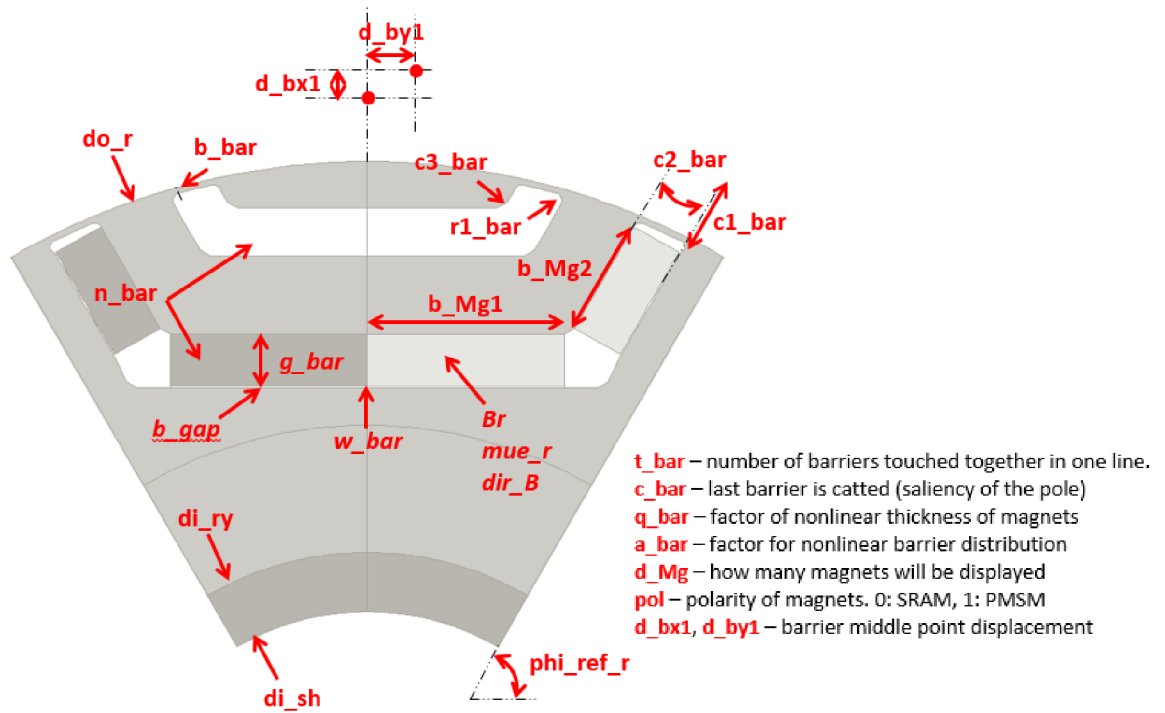


Fig. 4-5: SRAM1 geometry with the script parameters

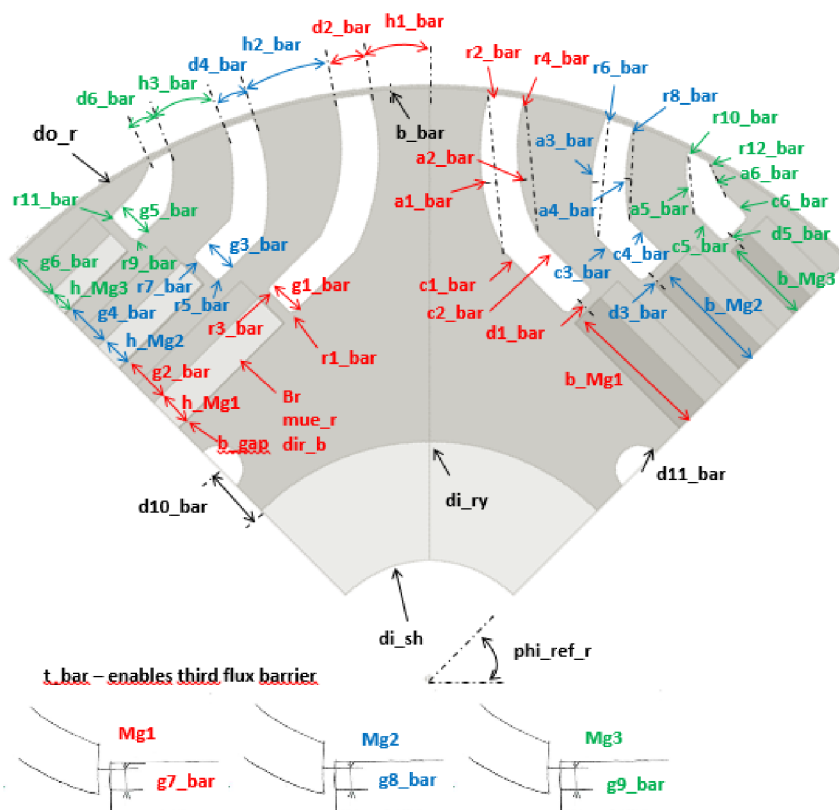


Fig. 4-6: SRAM2 geometry with the script parameters

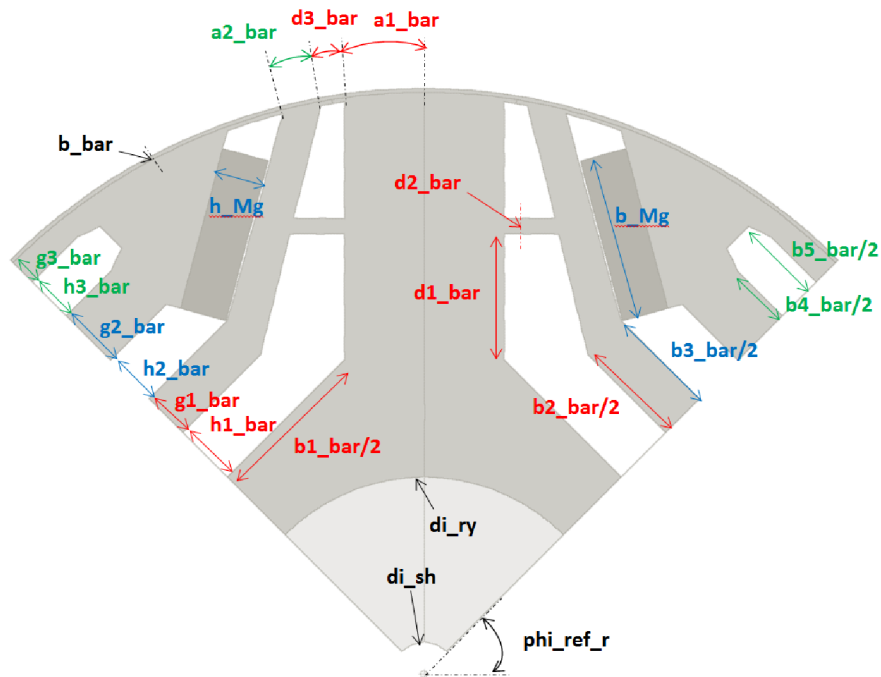


Fig. 4-7: SRAM3 geometry with the script parameters

The geometries presented above were created as they are listed in this thesis. The first one was created simply from the SRM geometry adding only the magnets into the flux barriers. Similar PMASR geometry can be found in paper [16]. The next two were created after literature research. The SRAM2 geometry is inspired by paper [17]. The last script was created to investigate and prove facts listed in [18]. All three scripts (geometries) will be tested and advantages and disadvantages will be presented hereafter.

5 MOTOR DESIGN

In this chapter PMASR design process will be described. All three geometries will be compared with ferrite permanent magnets. Optimal solution considering the chosen objectives will be found. Attention will be paid also to non-electric characteristics, such as mechanical strength. All the PA optimization results are presented in attachments, only important calculation results are included in this chapter.

5.1 Introduction

The SRAM design process starts with Baumüller's goal to find a low-cost alternative to its original SMPM motor, for the financial reasons and reasons listed in chapter 2.2. Because the goal is to replace motor we need to keep the original diameter dimensions and parameters which are listed in table below:

Table 1 - SMPM motor specifications

Rated output torque	6.7 Nm
Rated line-to-line voltage	400 V
Nominal speed	2450 rpm
Stator outer/inner diameter	135 mm
Number of slots/poles	12/10

The starting point where the design will start will be the stator, which will be used the same as in the original machine. It is known, that for different types of motor, different slot design and different types of winding are needed. Stator will need to be optimized as well. But for the first few steps the original stator will be used. Hence the first design attempt of PMASR machine will be with combination of slots and poles 12/10.

All calculations will be done in the FEMAG software, using finite element analysis. Models will be fed with constant current, terminal voltage will be calculated with FEA.

After the optimal model is found, FEA calculations will be compared with analytical model.

5.2 SRAM1 geometry, Q=12, 2p=10

Every geometry will developed over time. There are few objectives that help to evaluate if the certain change of parameter lead to better or worse results. Parametric analysis (PA) will be done on every geometry to discover new solutions with better characteristics. As objectives average torque M_{avg} , torque ripple M_{PP} , terminal line voltage U_L , power factor $\cos\varphi$, efficiency η and total harmonic distortion of line-line voltage THD_{LL} will be used. Also inductances in d and q axis

L_d and L_q with calculated saliency ξ and area of permanent magnets A_{PM} will be presented.

5.2.1 SRAM1 12/10 combination with one flux barrier per pole geometry

The initial geometry has only one flux barrier with magnet per pole. The first PA will be on two parameters d_{bx1} and d_{by1} , which affects flux barrier shape and placement inside the rotor.

In table (Tab. (A1)) in attachments comparison of initial and optimal d_{bx1} and d_{by1} values is shown. Changes of parameters d_{bx1} and d_{by1} boundaries were set from 0 to 10 with step equals to 5.

It is obvious, that combination $Q= 12$, $2p= 10$ and one flux barrier per pole gives unsatisfactory results ($M_{avg}= 4.7$ Nm). Initial model was optimized and except THD_{LL} and PM area all objectives improved. Flux barrier was moved closer to the rotor surface.

Considering the poor power factor was decided, that the combination of two flux barriers per pole with the same slots per pole and phase should be investigated. The theory was, that with higher amount of PM inside, the power factor would be higher.

5.2.2 SRAM1 12/10 combination with two flux barriers per pole geometry

In the first PA were parameters d_{bx1} and d_{by1} were changed again in the same interval as in the first PA. Results are in the table in attachments (Tab. (A2)).

Adopting the second flux barrier caused the power factor to be lowered. The second flux barrier has positive effect on THD_{LL} which is significantly lower. Initial model was again improved and the optimized model has better characteristics. Both barriers were shifted closer to the rotor surface.

In the second PA, parameters a_{bar} and q_{bar} were optimized. Those parameters affect flux barriers distribution and thickness. Both parameters were changed from 0.8 to 1.2 with step 0.2. When parameter a_{bar} is higher than 1, all barriers are slightly shifted closer to rotors outer diameter. If parameter q_{bar} is smaller than 1, second (outer) flux barrier is thinner. In attachments (Tab. (A3)) are results presented in the table.

Even the parameters a_{bar} and q_{bar} did not significantly improve the objectives in the model. Optimal model has a thinner outer barrier but the placement remained the same. Even though the script allows creating more than two flux barriers per pole, the pole area is not wide enough to try that. It is clear from the results that the combination 12/10 is far from being ideal for PMASR.

After calculations, the search for new slot per pole combination started. In literature [19] the author calculated combination 12/10 with NdFeB magnets with satisfactory results. That was proven by one calculation on optimal two flux barrier geometry with NdFeB magnets. Results of ferrite and NdFeB PMASR versions are in the table below.

Table 2 - Ferrite and NdFeB PMASR 12/10 versions with two flux barriers per pole comparison

Model			Ferrite	NdFeB
	Symbol	Unit		
Average torque	M_{avg}	[Nm]	4.047	9.189
Torque ripple	M_{pp}	[%]	15.23	9.01
Terminal voltage	U_1	[V]	165.92	190.92
Total harmonic distortion	THD _{LL}	[%]	17.53	9.98
Power factor	$\cos \varphi$	[-]	0.48	0.915
Efficiency	η	[%]	91.34	95.74
Direct axis inductance	L_d	[mH]	34.92	27.77
Quadrature axis ind.	L_q	[mH]	16.97	15.7
Magnetic saliency	ξ	[-]	2.1	1.8
PM area	A_{PM}	[mm ²]	587.4	587.4

In paper [10] the author also investigated three combinations for ferrite versions of PMASR, 27/6, 27/4 and 24/4. When achieving the same torque, the 27/6 ($q= 1.5$) combination had the shortest stack length. Let us note that all investigated combinations have slots per pole per phase number higher than 1, while first calculations done in this paper had this number lower than 1. For PMASR motor the number q has to be higher than 1, which was also proven in [19]. In this paper the author proposed various slots per pole combinations and compared them. None of those proposed combinations were nearly as good as the combination with $q=1.5$, even though skewing and various ripple reducing techniques were applied on the other combinations. Thus the next combination of slots and poles will be 27/6.

5.3 SRAM1 geometry, Q=27, 2p= 6

Model development will again start with one flux barrier per pole and the first PA will be the same as in 12/10 model.

With 27/6 model it will be possible to create more space for permanent magnets, which is in case of ferrite magnets very important.

After the very first calculation it was obvious that desired torque would be achieved, thus it was decided after conversation with the project manager, that air

gap will be lengthened to 0.5 mm. This lengthening should reduce THD_{LL} , thus the hysteresis rotor losses.

5.3.1 SRAM1 27/6 combination with one flux barrier per pole geometry

The first PA was performed with parameters d_{bx1} and d_{by1} in interval from -7.5 to 2.5 with step equals to 5. Results are shown in the table in attachments (Tab. (A4))

With 27/6 it was possible to achieve the desired torque with the same stator current as in the 12/10 combination. However the number of stator coil turns needed to be increased. Initial geometry was created by placing the permanent magnet as close to rotor surface as possible, which had good influence in 12/10 model. The initial model was found to be ideal.

5.3.2 SRAM1 27/6 combination with two flux barriers per pole geometry

The first calculations of 27/6 combination showed promising results. Calculated geometry achieved desired specifications and is incomparable with 12/10 optimal model. Torque ripple and total harmonic distortion has decreased significantly and both power factor and efficiency increased.

Again, two flux barriers per pole geometry were adopted and the same parametric analysis, within the same interval and step was done. Results of PA optimizing the d_{bx1} and d_{by1} parameters are presented in the table in attachments (Tab. (A5)).

The optimal model from the first PA has lower torque ripple, THD_{LL} and magnet area. In addition both efficiency and power factor increased, while almost the same average torque was achieved. Flux barriers with this combination d_{bx1} and d_{by1} are closer to the rotor surface than they were before the analysis.

The second PA was focused on parameters a_{bar} and q_{bar} , interval was set from 0.8 to 1.2 for both variables. Step was set to 0.2 and results are shown in the table in attachments (Tab. (A6)).

With this q_{bar}/a_{bar} combination, the flux barriers have the same thickness, but are placed slightly closer to the rotor surface. This PA results in decreasing the torque ripple, other objectives changed very slightly. Low terminal voltage allowed us to increase the number of turns in the stator coil, and lower the stator current. Results with original optimal model are presented in the table below.

Table 3 - Results of the number of turns and stator current modification on 27/6 combination with two flux barriers per pole

Model			Initial	Optimal
	Symbol	Unit		
Optimized parameter	N_c/I_s	[-/A]	26/5.2	30/4.4
Average torque	M_{avg}	[Nm]	7.255	7.247
Torque ripple	M_{pp}	[%]	2.95	3.14
Terminal voltage	U_1	[V]	170.04	186.73
Total harmonic distortion	THD_{LL}	[%]	2.8	3.1
Power factor	$\cos \varphi$	[-]	0.714	0.764
Efficiency	η	[%]	94.08	94.4
Direct axis inductance	L_d	[mH]	51.5	71.61
Quadrature axis ind.	L_q	[mH]	8.84	12.04
Magnetic saliency	ξ	[-]	5.8	5.9
PM area	A_{PM}	[mm ²]	876.5	876.5

Modifications resulted in slightly increasing efficiency and power factor and the THD_{LL} , torque ripple and magnetic saliency.

5.3.3 SRAM1 27/6 combination with three flux barriers per pole geometry

The pole area in 27/6 is broader, thus the three flux barriers per pole combination can be created and calculated. The first PA will modify the flux barrier shape and position through parameters d_{bx1} and d_{by1} . Results are presented in attachments (Tab. (A7)).

It is clear from the results, that combination with three flux barriers per pole is worse than previous combinations. With the same stator current developed torque is much lower with higher torque ripple and THD_{LL} . More parametric analysis will not be performed.

Both optimal models with one and two flux barriers per pole are very good. But after all the calculations, Baumüller Company requested to design an 8-pole motor. Since the 27/6 combination with q equals to 1.5 had such a good characteristics, the similar motor with the same q will be designed. For the 8-pole machine with $q= 1.5$ the number of slots will be 36.

5.4 SRAM1 geometry, Q=36, 2p= 8

SRAM1 geometry will be changed, to satisfy the customer request, to an 8-pole machine. This combination is better for calculations. Since two poles are always simulated, in 27/6 combination was necessary to generate one third of the

machine, in 36/8 motor it is reduced to one quarter. Thus the number of the elements in the model should be theoretically reduced by (8.33%). This will result in faster calculations, and number of steps will be reduced as well from 120 to 90, considering the step equals to 1°.

5.4.1 SRAM1 36/8 combination with one flux barrier per pole geometry

The process presented in 27/6 combination will be performed again with the same structure. Thus at first one flux barrier per pole combination will be used and d_{bx1} and d_{by1} analysis will be done. Interval of the PA was chosen for both variables from -5 to 0 with step 2.5. Results are presented in the table below in attachments (Tab. (A8))

In optimized geometry almost all objectives improved, only magnetic saliency got worse and PM area increased.

Compare to 27/6 one flux barrier per pole version optimized 36/8 geometry has slightly higher torque ripple (3.5 vs 2.34 %), lower efficiency (93.1 vs 94.17 %) and lower power factor (0.735 vs 0.75). Higher torque was achieved (8.1 vs 7.37 Nm). Other objectives remained very similar.

5.4.2 SRAM1 36/8 combination with two flux barriers per pole geometry

Similarly, on the two flux barriers per pole geometry two analyses will be done. The first one is to find optimal combination of d_{bx1} and d_{by1} in interval from 0 to 10 with step 5. PA results are the table in attachments (Tab. (A9)).

Optimal geometry has lower average torque, torque ripple, power factor and efficiency. Reduced was torque ripple and THD_{LL} and also PM area.

PA for a_{bar} and q_{bar} variables were both analyzed with step 0.2 from 0.8 to 1.2. Initial and optimal model is shown in table (Tab. (A10)).

Analogously to identical PA done on 27/6 combination, the torque ripple and PM area decreased. Compare to the 27/6 combination, lower torque ripple was achieved with higher terminal voltage.

5.4.3 SRAM1 36/8 combination with three flux barriers per pole geometry

Even though with 36/8 combination pole area reduced, the three flux barriers per pole combination will be investigated. Compared to the two flux barrier combination, the interval for d_{bx1} and d_{by1} needed to be reduced, because the pole area is smaller. Borders were chosen from 0 to 5 with step 2.5.

The results are presented in the table in attachments (Tab. (A11)). The first d_{bx1} and d_{by1} combination optimal solution for the three flux barriers per pole geometry was found. Despite the relatively high average torque, efficiency and power factor, the torque ripple and THD_{LL} is found to be the biggest disadvantage. Thus, like in 27/6 SRAM1 version, the three flux barriers are not ideal and two flux barriers version was chosen for further stator optimization.

In stator optimization the stator tooth width (w_{tooth}), stator slot opening (w_{so}) and stator slot opening height (h_{so}) were optimized. A sketch of two stator slots with description is on the figure below.

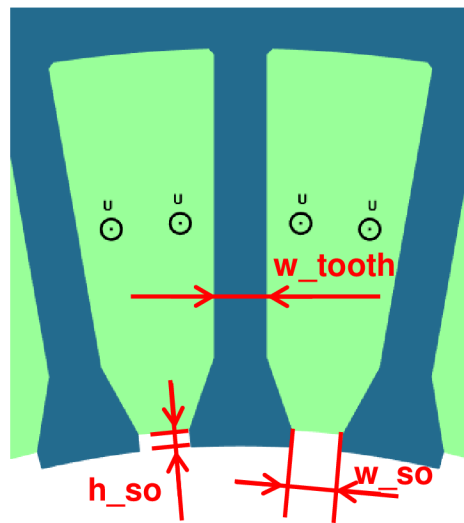


Fig. 5-1 - Stator slots with script parameters description

Optimized parameters were changed as they are presented in table below.

Table 4 - Results of the stator PA done on 36/8 combination with two flux barriers per pole

	Symbol	Unit	Range	Step	Optimal
Stator tooth width	w_{tooth}	mm	1 ÷ 6	1	3
Stator slot opening width	w_{so}	mm	1 ÷ 4	0.5	2.5
Stator slot opening height	h_{so}	mm	0.25 ÷ 1.75	0.25	1

Optimal parameter values were the same as the initial parameter, thus the objectives did not changed and the optimal model remained the same.

After the meeting with the technology department where the manufacture process was discussed a modification has been brought up. When the 27/6 model was designed, the air gap was lengthened to 0.5 mm to improve the torque ripple and THD_{LL} . For the sake of the efficiency and the power factor, the air gap length was set back to the original value of 0.3 mm. The motor needed to be recalculated. In the table below are listed three motor versions. The first one is the optimized version with the air gap length 0.5 mm, the second one is the same stator turns and current but with the air gap length 0.3 mm. In the third column are listed

objectives achieved with the optimized 36/8 model, modified number of stator coil turns and current to develop desired torque 6.7 Nm.

Table 5 – Final air gap modification and number of turns/current optimization on 36/8 combination

Model			Init. 0.5 mm air gap	Init. 0.3 mm air gap	Optim. 0.3 mm air gap
	Symbol	Unit			
Average torque	M_{avg}	[Nm]	7.957	8.489	6.779
Torque ripple	M_{PP}	[%]	2.8	3.03	3.18
Terminal voltage	U_1	[V]	183.71	208.06	176.93
Total harmonic distortion	THD_{LL}	[%]	2.3	5.2	4.9
Power factor	$\cos \varphi$	[-]	0.729	0.739	0.763
Efficiency	η	[%]	93.15	93.69	94.14
Direct axis inductance	L_d	[mH]	44.98	55.07	51.41
Quadrature axis ind.	L_q	[mH]	7.86	10.31	8.69
Magnetic saliency	ξ	[-]	5.7	5.3	5.9
PM area	A_{PM}	[mm ²]	787.6	787.6	787.6

Both efficiency and power factor were improved, with significant THD_{LL} rise. SRAM1 model is thus optimized by parametric analyses and the next SRAM version will be calculated and then compared with SRAM1. After selecting the best version the optimization by artificial intelligence will be performed.

5.5 SRAM2 geometry, $Q_s = 36$, $2p = 8$

The SRAM1 design development has shown some design keys. For example, three flux barriers geometry results in high torque ripple and the number of slots per pole per phase is optimal when $q = 1.5$. Thus the requested 8 pole motor with $q = 1.5$ will be considered.

5.5.1 SRAM2 36/8 combination with two flux barriers per pole geometry

Since the SRAM2 geometry does not allow to generate geometry with only one flux barrier and three flux barriers geometry results in the highest torque ripple, only two flux barriers per pole geometry will be investigated.

After the initial geometry was set with the optimized stator from the SRAM1 model, the optimization process could start.

The first two parameters which were chosen to be optimized were $g2_bar$ and $g4_bar$. Those two parameters affect the distance between two magnets, between outer magnet and rotor surface respectively. Parameter $g2_bar$ was changed in the interval from 1.1 to 2.1 with step 0.25 when $g4_bar$ parameter had its boundaries set from 0.8 to 1.6 with step 0.2. Results from this PA are presented in the table in attachments (Tab. (A13)):

Optimized geometry had magnets shifted closer to each other and both magnets are moved closer to the rotor surface. This geometry change resulted in higher average torque with higher ripple, but total harmonic distortion decreased by 2%. Slight decrease is noted in the power factor.

The second PA affects the width of flux barriers top ends, by parameters $d2_bar$ and $d4_bar$, where the first parameter is connected with the bottom and the second flux barrier. Both parameters were changed with step equals to 0.2 and boundaries were set to $1.4 \div 2.2$ mm, $0.6 \div 1.4$ mm respectively. Results of optimization are in the table in attachments (Tab. (A14))

Optimization of those parameters increased average torque and decreased the torque ripple and total harmonic distortion. Other objectives values remained almost the same. The optimized bottom flux barrier top end was after PA wider, whereas the top flux barrier top end resulted to be thinner.

The next parameters that were intended to be optimized are parameters controlling the bottom horizontal shift of flux barriers $g7_bar$ and $g8_bar$. The interval for optimization was chosen the same for both parameters and it is from -0.25 mm to 0.25 mm. Parameters were changed with step 0.25 mm, where negative value means that the bottom end is shifted further from the rotor surface. The initial values were found to be optimal, thus the values of parameters remained $g7_bar = 0.25$ and $g8_bar = 0$.

Since the optimal bottom end placement is found, the next PA will focus on the top end placement. The placement is controlled by parameters $h1_bar$ and $h2_bar$ whose optimal values will be investigated. Both parameters had their optimization boundaries set to 1.5 mm and 2.5 mm and were changed with step 0.25 mm. The results are shown in the table in attachments (Tab. (A15))

The flux barriers top ends placement affect torque ripple. The optimized parameters have lowered the torque ripple by 4%. The other objectives values remained almost the same.

The last parameters that could improve the geometry are the flux barriers radiuses. All radiuses can be adjusted by parameters $a1$ - $a4_bar$, where $a1$ and $a3$ bar parameters control inner radiuses. Optimization boundaries and steps with each parameter was changed are listed in the table below.

Table 6 - Optimization parameters for flux barriers radiuses

	Symbol	Unit	Range	Step
First flux barrier outer radius	a1_bar	mm	1 ÷ 1.8	0.2
First flux barrier inner radius	a2_bar	mm	0.7 ÷ 1.5	0.2
Second flux barrier outer radius	a3_bar	mm	0.5 ÷ 1.3	0.2
Second flux barrier inner radius	a4_bar	mm	0.1 ÷ 0.9	0.2

Optimized parameters with calculated objectives are shown in the table in attachments (Tab. (A15)).

Only the second flux barrier inner radius was optimized, the other three were optimal in the initial model. The change improved torque ripple slightly, THD_{LL} and magnetic saliency increased lightly.

All rotor parameters that could have significant effect on either average torque or torque ripple have been optimized. Thus the optimization of the stator parameters remains. The parameters that will be optimized are the same as in SRAM1 optimization process, plus two more parameters will be investigated.

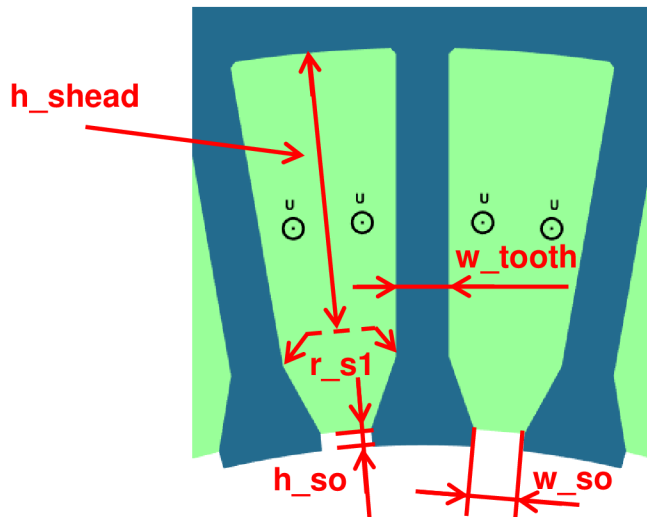


Fig. 5-2 - Stator slots with script parameters description

Table 7 - Results of the stator PA done on 36/8 combination with two flux barriers per pole

	Symbol	Unit	Range	Step	Optimal
Stator tooth width	w_tooth	mm	2 ÷ 4	0.5	3.5
Stator slot opening width	w_so	mm	1 ÷ 4	0.5	2.5
Stator slot opening height	h_so	mm	0.25 ÷ 1.75	0.25	1
Inner slot corner radius	r_s1	mm	1 ÷ 2	0.25	1.5
Slot head height	h_shead	mm	1 ÷ 3	0.25	2

Table 8 - Results of the stator PA done on SRAM2 36/8 combination with two flux barriers per pole

Model			Initial	Optimal
	Symbol	Unit		
Average torque	M_{avg}	[Nm]	6.597	6.755
Torque ripple	M_{PP}	[%]	8.0	7.7
Terminal voltage	U_1	[V]	169.8	174.44
Total harmonic distortion	THD_{LL}	[%]	8.2	6.9
Power factor	$\cos \varphi$	[-]	0.750	0.748
Efficiency	η	[%]	94.24	93.9
Direct axis inductance	L_d	[mH]	52.21	53.65
Quadrature axis ind.	L_q	[mH]	10.97	11.12
Magnetic saliency	ξ	[-]	4.8	4.8
PM area	A_{PM}	[mm ²]	864	864

Thanks to the PA, the average torque increased and torque ripple decreased. Because the stator tooth width increased, the current density increased as well. That causes the copper losses to increase and efficiency to decrease.

5.6 SRAM3 geometry, $Q_s = 36$, $2p = 8$

Similarly to the SRAM2 geometry, the SRAM3 geometry will be developed as an 8-pole machine with 36 stator slots, thus the number of slots per pole per phase remains $q = 1.5$.

Initial geometry was chosen, and is ready to be optimized. The first two parameters are bottom and top width of the first (bottom) flux barrier. Widths are controlled by parameters $b1_bar$ and $b2_bar$. Boundaries were set to $15 \div 20$ mm and $10 \div 18$ mm respectively. Both parameters were changed with step 1 mm. Results are presented in attachments (Tab. (A16)).

Optimized bottom flux barrier has a wider bottom, but thinner sides. Average torque value remained the same, while the torque ripple lowered significantly. All the other objectives changed only slightly, beside the voltage, which rose by 5 V.

The second PA is focused on the bottom width of the second flux barrier. This width is controlled by $b3_bar$ parameter. Step for the operation was set to 1mm and parameter was changed from 7 to 15. The initial value of $b3_bar$ parameter was found optimal, thus the values of the objectives remained the same.

Next PA is focused on thickness and placement of iron ribs, created in the bottom flux barrier's sides. The ribs are created symmetrically along the q -axis. The placement is controlled by parameter $d1_bar$, while the thickness is set by

parameter $d2_bar$. The first parameter was changed with step 5 mm and from 5 to 10 mm, measured from the bottom of the flux barrier. Thickness value was changed from 0.5 to 1.5 mm with step 0.5 mm (Tab. (A17)).

Optimization decreased the torque ripple, while average torque remained almost the same or improved slightly.

All PA done on the rotor from this point had not improved the model, thus stator optimization begun. The same set of stator PA like in SRAM2 optimization was performed. The optimal stator for SRAM2 geometry was found to be optimal also for the SRAM3 geometry. Because the demanded torque was not achieved with the initial stator current, it needs to be increased. The initial and optimized setup for reaching the average torque of 6.7 Nm is shown in the table below.

Table 9 - Results of the stator SRAM3 PA done on 36/8 combination

Model			Initial	Optimal
	Symbol	Unit		
Optimized parameter	I_s	[A]	4.5	5
Average torque	M_{avg}	[Nm]	5.933	6.718
Torque ripple	M_{PP}	[%]	4.34	4.55
Terminal voltage	U_1	[V]	182.59	191.75
Total harmonic distortion	THD_{LL}	[%]	8.5	9.1
Power factor	$\cos \varphi$	[-]	0.633	0.616
Efficiency	η	[%]	92.73	92.41
Direct axis inductance	L_d	[mH]	51.83	48.94
Quadrature axis ind.	L_q	[mH]	19.84	19.29
Magnetic saliency	ξ	[-]	2.6	2.5
PM area	A_{PM}	[mm ²]	495.6	495.6

With SRAM3 geometry it is possible to achieve demanded torque, but with lower efficiency and mainly with poor power factor and high total harmonic distortion. In the next chapter all three geometries will be compared to see which one is the best for the wanted parameters.

5.7 Comparison of the geometries

All optimal SRAM geometries can be found in the table below. Let us note, that the stack length of all three machines is the same, also the number of turns is the same.

Table 10 – Comparison of optimized geometries

Model			SRAM1	SRAM2	SRAM3
	Symbol	Unit			
Feeding current	I_s	[A]	4.4	4.4	5
Average torque	M_{avg}	[Nm]	6.779	6.755	6.718
Torque ripple	M_{PP}	[%]	3.18	7.7	4.6
Terminal voltage	U_1	[V]	176.93	174.44	191.75
Total harmonic distortion	THD_{LL}	[%]	4.9	6.9	9.1
Power factor	$\cos \varphi$	[-]	0.763	0.748	0.616
Efficiency	η	[%]	94.14	93.9	92.41
Direct axis inductance	L_d	[mH]	51.41	53.65	48.94
Quadrature axis ind.	L_q	[mH]	8.69	11.12	19.29
Magnetic saliency	ξ	[-]	5.9	4.8	2.5
PM area	A_{PM}	[mm ²]	787.6	864	492.8

All models have been calculated to develop similar average torque. The SRAM3 geometry in comparison is the least suitable because of the high THD_{LL} and relatively low power factor. The efficiency is also the lowest of all three models.

SRAM1 geometry compared to the SRAM2 model has about 58.7% lower torque ripple, lower THD_{LL} by 2%. Efficiency and power factor are also higher in SRAM1. SRAM1 also achieved the demanded torque with smaller amount of PM used.

In the previous calculations M330-35A steel has been used for the rotor and stator iron sheet material. Because the SRAM machine calculations were done to develop cheaper machine than SMPM motor, all three versions will be recalculated for cheaper steel M470-50A.

B-H curves for both materials are presented on figure below. Data were used from datasheets.

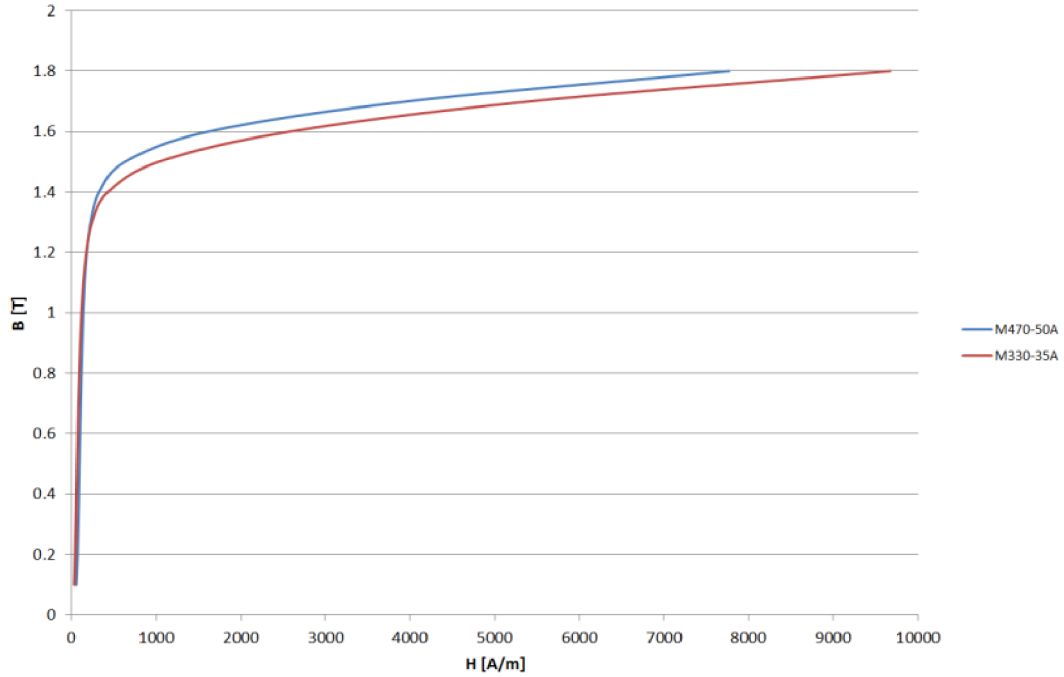


Fig. 5-3: M470-50A and M330-35A B-H curves comparison

The B-H curves comparison is showing, that with the same magnetic field strength it is possible to achieve higher mag. flux-density using the M470-50A steel. Higher flux-density means higher torque, the supplying current needs to be lowered. Results of all three models with M470-50A steel are presented in the table below.

Table 11 - Results of the optimized geometries for M470-50A iron

Model			SRAM1	SRAM2	SRAM3
	Symbol	Unit			
Average torque	M_{avg}	[Nm]	6.797	6.745	6.756
Torque ripple	M_{PP}	[%]	3.7	7.4	4.9
Terminal voltage	U_1	[V]	194.91	177.26	193.74
Total harmonic distortion	THD_{LL}	[%]	3.8	6.1	8.7
Power factor	$\cos \varphi$	[-]	0.764	0.751	0.619
Efficiency	η	[%]	93.2	93.5	91.25
Direct axis inductance	L_d	[mH]	62.35	55.74	49.96
Quadrature axis ind.	L_q	[mH]	10.02	11.03	19.5
Magnetic saliency	ξ	[-]	6.2	5.1	2.6
PM area	A_{PM}	[mm ²]	787.6	864	492.8

The change of the material had a different impact on models. All three models have the same power factor with M470-50A iron compare to M330-35A. In all three models efficiency the THD_{LL} decreased slightly. Overall improvement has shown only SRAM2 model.

All six models were discussed at Baumüller and considering the mechanical strength the SRAM2 with M330-35A iron was model chosen. SRAM2 model has relatively high torque ripple and the highest PM area of all three models.

Unfortunately, the FEA calculation in FEMAG does not include the coil overlaps and consider the copper fill factor equals to $k_{p,Cu} = 0.4$. After the discussion with the supervisor in Baumüller the coil overlap was estimated to be $l_b = 68$ mm. Because the stator area is relatively small, the manufacture ability for copper fill factor is set $k_{p,Cu} = 0.35$. Thus some of the recalculated objectives are:

Table 12 Recalculated objectives for new copper fill factor and considering the coil overlap

Model			Original	Recalculated
	Symbol	Unit		
Terminal voltage	U_1	[V]	177.26	181.52
Power factor	$\cos \varphi$	[-]	0.751	0.746
Efficiency	η	[%]	93.2	91

6 MECHANICAL ANALYSIS

In this chapter the mechanical strength of the chosen model will be investigated. The calculation will be performed in ANSYS software using FEM. Results of the analysis will be presented on a sketch of the simulated part of iron sheet.

6.1 Introduction

Because the SRAM2 geometry was chosen to be investigated further, the mechanical analysis will be performed just on this model. The mechanical analysis will be done with ANSYS software using the FEA. The software was founded in 1970 and the company develops markets and supports engineering simulation software [20].

The advantage of this software is that the materials library is big, so a lot of commonly used materials are preset. The only material that needed to be added was the magnet material.

6.2 Static structural analysis

The analysis that will be performed in the ANSYS software is the “Static structural” analysis. In this analysis it is possible to investigate rotor’s strength towards the centrifugal force during in the nominal point. It is expected that the weakest places in the geometry will be probably the island above the second (outer) magnet.

3D mechanical analysis will be performed on one sheet. Using the geometric symmetries it is possible to analyze only two poles. Therefore smaller mesh elements can be generated while the same computing power remains and more accurate result will be gained.

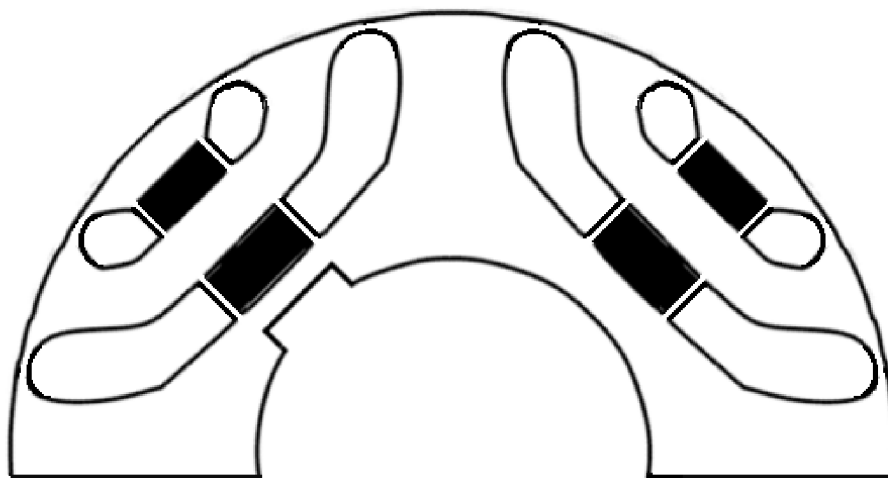


Fig. 6-1 Sketch of the investigated system in Static structural analysis [28]

6.3 Setup

All parts needed for the analysis were created in the software Solidworks. The analysis itself needs some input information that needs to be provided to get the correct result. The structure of the input info, thus the whole analysis, is on the picture below.



Fig. 6-2 Analysis structure

After the material initialization the materials are assigned with the parts. The magnets bonds are chosen to be “Frictionless”. The back of the plate and the sides of the sheet are “locked” so they cannot move in axes they would not move in real situations. Results of the static structure analysis are presented on sketch below.

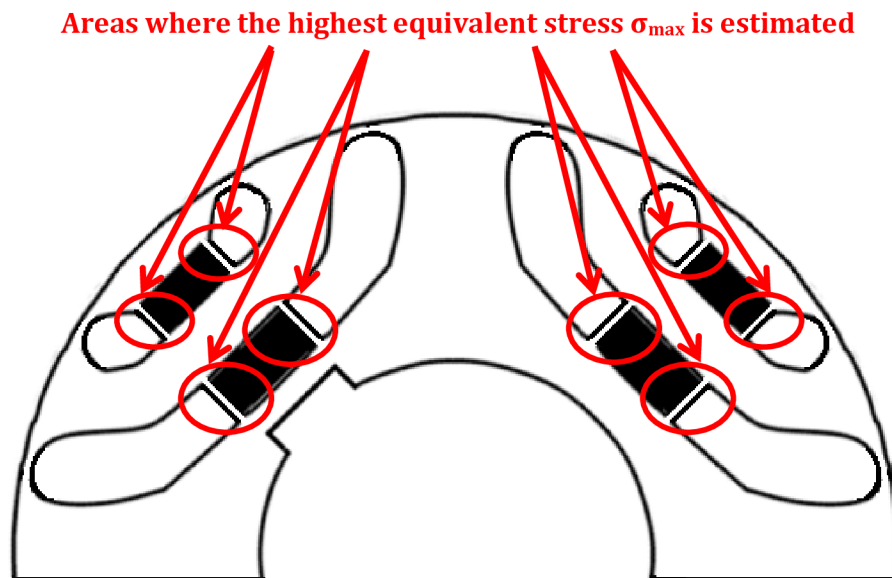


Fig. 6-3 Estimated areas with the highest equivalent stress (Sketch from [28])

6.4 Mechanical analysis summary

Areas, where the highest equivalent stress was calculated are highlighted. The highest calculated stress was $\sigma_{max}= 9.0825$ MPa and the weakest places in the geometry are ribs around the magnets. Iron sheets are made of M330-35A electrical steel, which has yield strength $\sigma_{steel}= 315$ N/mm² [29]. The yield strength unit N/mm² corresponds with the yield strength MPa unit. The calculated value can be then directly compared with the value from the datasheet. It is obvious, that the designed geometry is strong enough to sustain the centrifugal force in the nominal point (9.0825 MPa \ll 315 MPa).

After mechanical analysis thermal analysis would be usually performed. Because the previous design was more time consuming, than it was originally assumed the thermal analysis will be skipped. Thermal analysis was performed for the SRAM1 6-pole version before the requirement for the 8-pole machine was received. No sign of overheat was found, thus it was expected to be the same for this model.

7 FEA AND ANALYTICAL MODEL COMPARISON

This chapter presents both the FEA and analytical model and with their advantages and disadvantages. Comparison of the calculated FEA and analytic model torque behavior will be presented hereafter. Differences and improvements will be discussed.

7.1 Introduction

At first it is important to sum up vital facts about both calculations that could affect the results.

Firstly the FE analysis will be discussed. Because the FEA was used before the analytical model was programmed, the scripts were heavily improved over the months. The biggest problems appeared in mesh generation. After nearly a month of performing calculations, crucial bugs in mesh generation were found. Considering only SRAM2 script two areas in iron ribs in each flux barrier, where mesh was not generated correctly, were found. The first one was found in rib between the magnet and flux barrier and the second at the flux barrier end. Elements were made smaller and results were made more accurate. Similar issues were found also in SRAM1 and SRAM3 models. Because a lot of time was spent improving the FEA model, the FEA results are considered to be more accurate. Let us note that the FEA calculation in 8-pole motor version takes about 5-10 minutes to calculate depending on the number of steps in the calculation.

On the other hand the analytical model was programmed later only to confirm the FEA results. The author is grateful to Mr. Massimo Barcaro, who provided the codes for simplified SRM model. Analytical model code is written in Matlab software and still probably includes few bugs. Even though the main part of the code was not written by the author, few improvements needed to be done. The original analytical model was used for integer winding and a machine without magnets. The parts of the code were added and different harmonics in electric loading were considered. Thanks to the very valuable publications [20] done by Mr. Nicola Bianchi and his colleagues and his personal communications, the improvements were successfully adopted. Analytical model magnetic and geometrical simplifications that were considered are:

- replaced stator slots by conductive sheet
- geometry of the flux barrier expressed by equivalent thickness and length (which is not equivalent in FEA model)
- magnetic bridges at the flux barriers end are neglected
- magnetic bridges between the PM and flux barrier are neglected
- irons magnetic reluctance is considered 0

The analytical model still needs a lot of work to adopt it on all SRAM geometries presented in this thesis. Now the code needs to input flux barrier angles, thicknesses and lengths, but the goal is to input the same set of parameters as in FE model and get ideally the same result. With the analytical model it takes around 5s to calculate the result. Primarily the analytical model will be used to quickly determine the basic dimensions and currents to achieve the desired torque with optimal torque ripple. After this thesis the analytical model will be extended with artificial intelligence optimization algorithm to achieve fast optimization for chosen geometry.

The SRAM2 optimal geometry torque calculated with FE and analytical method was compared. From the literature [2] it is obvious that it is enough to calculate in analytical model only 1/3 of the pole, thus in our case 15° mech. Comparison of both calculated torques is shown on the picture below.

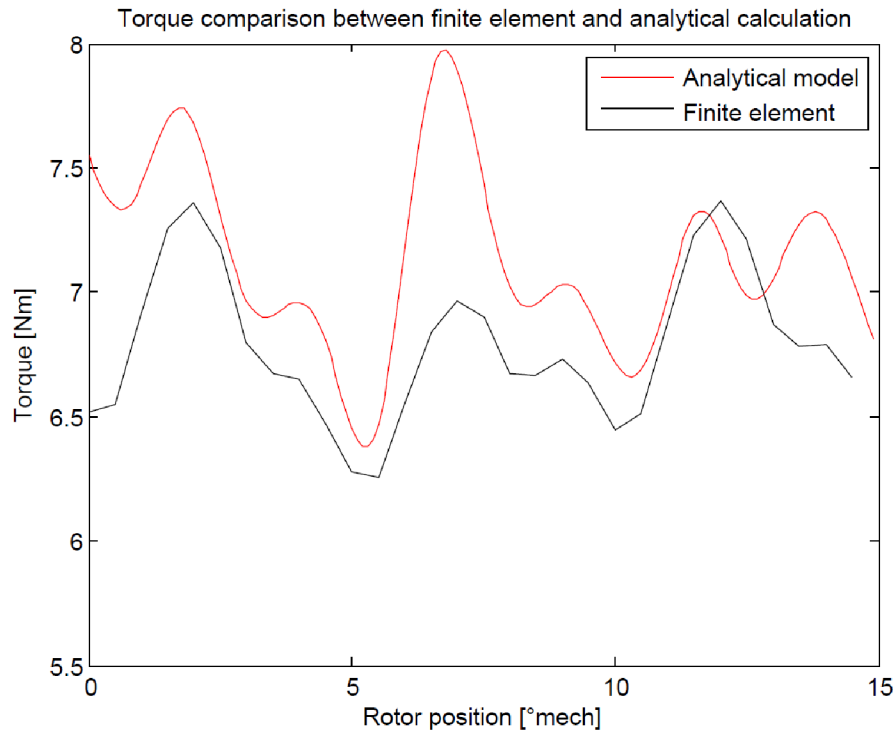


Fig. 7-1 Torque behavior comparison between FEA and analytical calculation

Regarding the simplifications that were considered only in the analytical model, a relatively good agreement is found. In literature [2] the author presented an even better agreement between calculated torques. But let us note that in literature both models are simplified similarly, while FEA model in this thesis is not simplified. Taking this into account the final result is solid. Significant difference between compared torques is found around the third torque peak. It is assumed that it is caused by thinner second flux barrier end that is much thinner than the assumed equivalent thickness.

8 FEA AND PROTOTYPE COMPARISON

In this chapter the FEA results and the manufactured prototype will be compared. Possible differences and cause of the differences will be discussed and eventual solution will be investigated.

8.1 Results comparison

The prototype was manufactured according to the calculated dimensions and parameters. A manufactured prototype was then tested in the laboratory by Baumüller Company. Measured results are compared in the table below.

Table 13 FEA and prototype results comparison

Model			FEA	Prototype	Difference in %
	Symbol	Unit			
Stator current	I_S	[A]	4.4	4.408	0.182%
Average torque	M_{avg}	[Nm]	6.745	5.46	-19.1%
Terminal voltage	U_1	[V]	181.52	165.815	-8.65%
Power factor	$\cos \varphi$	[-]	0.746	0.740	-0.8%
Efficiency	η	[%]	91	86.2	-5.3%
PM temperature	ϑ_{PM}	[°C]	80	119.8	49.8%

From the table it is obvious, that the designed motor did not achieve the calculated torque. The biggest differences are found in average torque (-19.1%) and in PM temperature (+49.8%).

Before any improvements to the geometry will be done, it is vital to find the main cause of the magnet high temperature. The high temperature might be connected with the low average torque.

After discussion two possible causes of high temperature came up:

- MMF harmonic in permanent magnets, causing eddy current losses
- Influence of the laser cutting procedure.

Temperature in permanent magnets was measured from the PM flux linkage. Firstly the rotor rotating with the dynamometer and the voltage induced in stator coils were measured, thus the flux linkage when the PM's are cold was determined. After the temperature became stable and the torque and all the objectives were measured, the source was disconnected and the voltage was measured again. With the measured flux linkages and PM Datasheet the temperature was calculated.

Used measuring equipment is shown in the table in attachments (Tab. (A18)) and photographs of the testing bench are presented on images below.

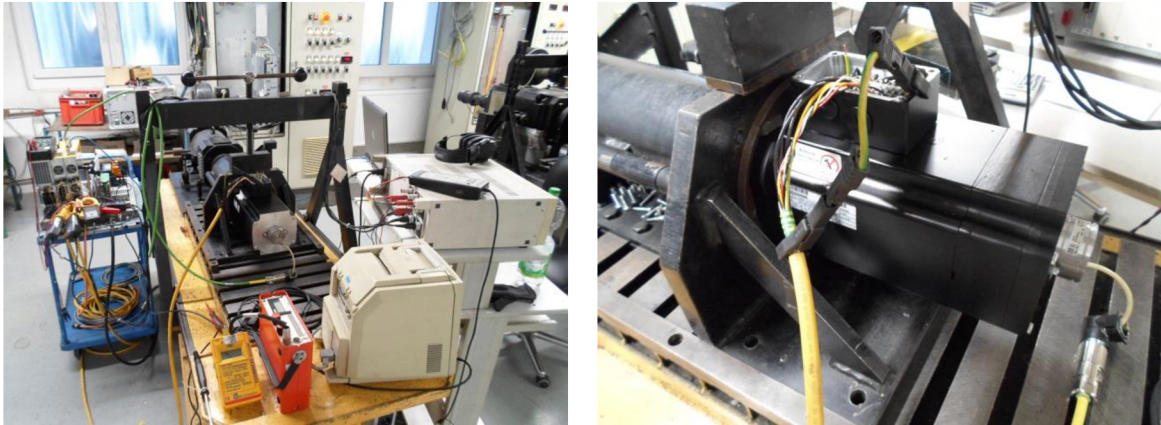


Fig. 8-1 Layout of the test bench and tested motor

8.2 MMF harmonics in permanent magnets

The high temperature in magnets might be caused by MMF harmonics causing the eddy current losses in PM. Few papers were written on this problem [21], [22], [23] last two regarding the IPM machines. Even though the rotor eddy currents might cause PM to overheat it is highly improbable to happen in ferrite PMASR machine. The ferrite magnets used in model and prototype are located in the branch of ferrimagnetic materials. These kinds of materials are sometimes called ceramics magnets [24]. The ferrite magnets properties are therefore similar to the ceramics magnets. On the picture below ferrimagnetic material is presented along with the other magnetic materials.

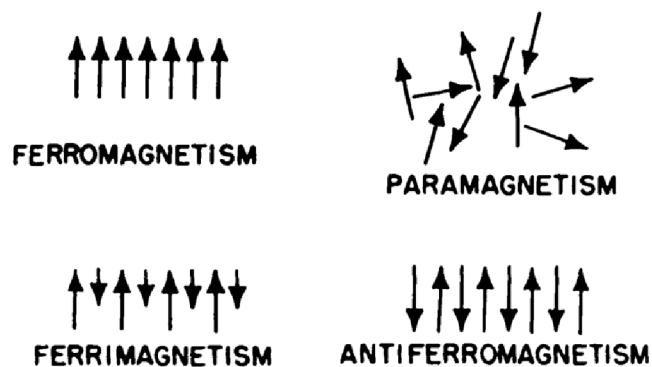


Fig. 8-2 Magnetic materials [26]

Magnetic atomic moments have parallel alignment similarly to the ferromagnetic material, but the orientation is not always in the same direction. The ferromagnetic materials electric resistance is much higher than in ferromagnetic materials, e.g rare-earth magnets. This is the reason why the eddy current losses are negligible in ferrite magnets [25]. Hence the PM overheat could not be caused by eddy currents.

8.3 Laser cutting influence on magnetic properties

It was discussed in previous chapter why the magnets cannot be overheated by themselves, hence the heat must come from outside of the magnets. The magnets are inserted in the flux barriers in close touch with the iron sheets, which might be the source of the heat.

Sheets were catted by laser beam and the magnetic properties of the iron sheets are influenced by this procedure. In literature [21] is described how and why the properties changed.

In the literature [21] two common procedures of cutting the iron sheets are compared: the laser cutting and the mechanical cutting. The first one degrades the material by inducing the thermal stress near the cutting line. The second one degrades the material near the cutting line by causing the mechanical deformation [21]. In picture below is the magnetic properties change is shown on hysteresis loop.

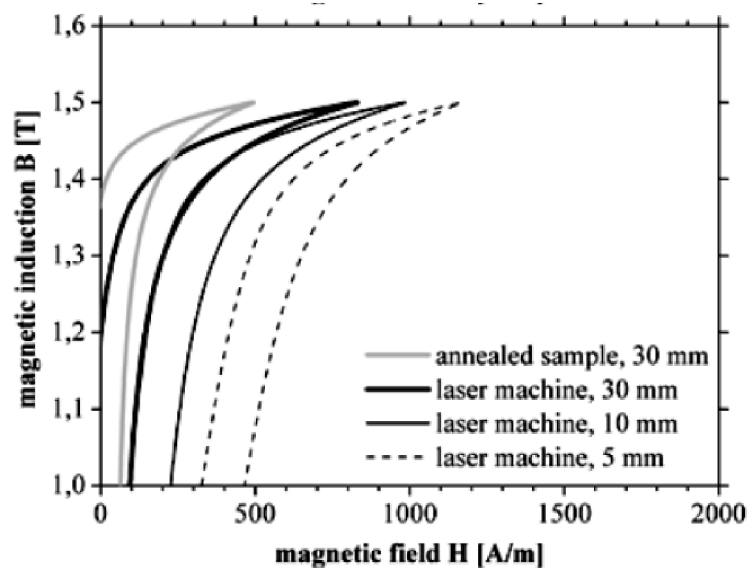


Fig. 8-3 Laser cutting influence on material [21]

Since the magnetic field to achieve the same mag. induction has to be stronger, the material permeability had to decrease.

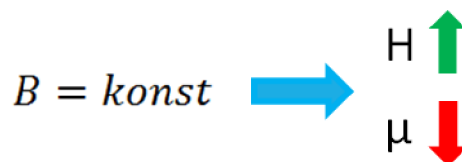


Fig. 8-4 Relationship between flux density and magnetic intensity behavior

Because the permeability decreased, the magnetic inductance in both axes had to decrease as well. Because the inductance decreased, the inductance

difference between d and q axes is also reduced, causing the reluctance torque to become smaller. For easier following of those logical steps the image below was created.

$$M_{mot} = \frac{3}{2} \cdot p \cdot [\psi_{PM} \cdot i_d + (L_d - L_q) \cdot i_d \cdot i_q]$$

Fig. 8-5 Concluded torque reduction

In the literature [21] the influence was investigated on the sheets from 5 to 30 mm and then compared with the annealed sample, where the original properties should be restored. The laser cutting influence on electric steel is remarkable. It is also noted, that the influence on thinner samples might be even stronger [21]. The distance between the magnets in the manufactured prototype is less than 2 mm, therefore the material has to be deformed even more. The author also noted, that significant temperature rise in the investigated samples was observed [21]. This was proven by the author also in [27], where in unannealed materials higher losses were observed. Thus the laser cutting process explains both the torque decrease and the temperature rise.

On Fig. 8-3 are samples with different width compared with annealed sample. Fig. 8-3 also shows that the magnetic properties could be restored with the stress relief annealing procedure.

9 CONCLUSION

This thesis deals with the permanent magnet assisted reluctance motor design problematics. The whole design process was proposed and should provide good background for future motor design purposes.

The second chapter consists of the motor presented with the potential range of applications and motor geometry description. Motor advantages and disadvantages are presented and compared to conventional SRM and also SMPM motors explaining the work's purpose.

After the introduction the electro mechanic conversion is presented, explaining the motor function principle. Then the mathematical point of view is taken and the machine is described in d-q axes that results with the torque equations. Motor developed torque consist of two parts. The first part is developed by inductance saliency and the second by permanent magnets. Considering the stable state, the PM improves the power factor, which is described in chapter 2.5.

Next chapter is focused on simplified analytical model for two flux barriers per pole. The analytical model was then programmed in Matlab code and the results are presented. Analytical model brings good background for potential code extending to more flux barriers per pole in future. The code will be extended in the near future to provide even more satisfactory results. Code will be also updated to form when the analytical calculations input parameters will be the same as FEA for models.

In fourth chapter the finite element method is presented with the software and LUA scripts for generating the model. Despite the chapter length the biggest part of the time was spent on programming and debugging the scripts for the geometry generation. Even though more than 4 months were spent on improving the scripts, a few tweaks are still needed to be done.

The most important part of this work is presented in chapter 5, where the development process is presented. The chapter conclude with ideal slots per pole per phase combination $q= 1.5$. This combination is ideal for ferrite version of the machine. It is proven, that for the rare-earth magnets the 12/10 combination might be use to bring satisfactory results. For ferrite version it is concluded, that the two flux barriers per pole is ideal for this axis height. It cannot be said that there is a general precept for the magnet position or flux barrier shape. It is different for every geometry and axis height. Only one general design rule came up during the process, that permanent magnets should not be equally wide. Equal width leads to high torque ripple. The flux barriers ends have a major effect on the final torque ripple behavior. This is proven by the analytical model, where the flux barrier ends angles are used as input parameter.

After the electromagnetic design the mechanical analysis was done on chosen geometry. The chosen geometry was proven by FEA software Ansys to be mechanically strong enough to sustain the centrifugal force of the nominal speed. Thermal analysis was not done expecting the similar result achieved on 6-pole machine, where no overheating problems were found.

In seventh chapter both FE and analytical analysis were compared. Good agreement between the two methods was found even though the simplifications were considered only in the analytical model.

In the last chapter the FE model was compared with the manufactured prototype. The measured result was that desired torque was not achieved with the designed motor. The author concluded that the cause was not the higher MMF harmonics in the PM, but in the manufacturing technology. The manufactured process used for steel shaping was the laser cutting. The laser cutting degrades the iron material properties resulting in reduced torque and increased PM temperature. The magnetic properties could be restored by annealing of the material [21].

The model was then recalculated and a new version of the prototype that will be manufactured was designed after this thesis was written. In the new prototype it is assumed to use an annealing process expecting to get better characteristics with the second version of the motor.

Bibliography

- [1] KOSTKO, J. K. Polyphase reaction synchronous motors. Journal of the American Institute of Electrical Engineers [online]. 1923, 42(11), 1162-1168 [cit. 2016-09-06]. DOI: 10.1109/JoAIEE.1923.6591529. ISSN 0360-6449.
Dostupné z: <http://ieeexplore.ieee.org/lpdocs/epic03/wrapper.htm?arnumber=6591529>
- [2] BARCARO, Massimo. Design and Analysis of Interior Permanent Magnet Synchronous Machines for Electric Vehicles. Padova, 2011. Doctoral thesis. Università degli studi di Padova. Supervisor Ch.Mo Prof. Nicola Bianchi.
- [3] VARTANIAN, Robert, Yateendra DESHPANDE a Hamid A. TOLIYAT. Performance analysis of a ferrite based fractional horsepower permanent magnet assisted SynRM for fan and pump applications. In: 2013 International Electric Machines & Drives Conference [online]. IEEE, 2013, s. 1405-1410 [cit. 2016-09-18]. DOI: 10.1109/IEMDC.2013.6556321. ISBN 978-1-4673-4974-1.
Dostupné z: <http://ieeexplore.ieee.org/document/6556321/>
- [4] ARMANDO, Eric, Paolo GUGLIELMI, Michele PASTORELLI, Gianmario PELLEGRINO a Alfredo VAGATI. Performance of IPM-PMASR Motors with Ferrite Injection for Home Appliance Washing Machine. In: 2008 IEEE Industry Applications Society Annual Meeting [online]. IEEE, 2008, s. 1-6 [cit. 2016-09-18]. DOI: 10.1109/08IAS.2008.19. ISBN 978-1-4244-2278-4.
Dostupné z: <http://ieeexplore.ieee.org/lpdocs/epic03/wrapper.htm?arnumber=4658807>
- [5] VAGATI, A., G. PELLEGRINO a P. GUGLIELMI. Comparison between SPM and IPM motor drives for EV application. In: The XIX International Conference on Electrical Machines - ICEM 2010 [online]. IEEE, 2010, s. 1-6 [cit. 2016-09-18]. DOI: 10.1109/ICELMACH.2010.5607911. ISBN 978-1-4244-4174-7.
Dostupné z: <http://ieeexplore.ieee.org/lpdocs/epic03/wrapper.htm?arnumber=5607911>
- [6] BARCARO, Massimo a Nicola BIANCHI. Interior PM Machines Using Ferrite to Replace Rare-Earth Surface PM Machines. IEEE Transactions on Industry Applications [online]. 2014, 50(2), 979-985 [cit. 2016-09-19]. DOI: 10.1109/TIA.2013.2272549. ISSN 0-093-9994. Dostupné z: <http://ieeexplore.ieee.org/lpdocs/epic03/wrapper.htm?arnumber=6556949>
- [7] BÁRTA, Jan. Návrh a optimalizace synchronního reluktančního motoru. Brno, 2014. Diplomová. Vysoké Učení Technické v Brně. Vedoucí práce Doc. Ing. Čestmír Ondrůšek, CSc.
- [8] ONDRŮŠEK, Čestmír. Dynamika elektromechanických soustav. Brno, 2013. Skriptum. FEKT VUT v Brně.

- [9] DEGANO, Michele, Hanafy MAHMOUD, Nicola Bianchi and Chris GERADA. Synchronous Reluctance Machine Analytical Model Optimization and Validation Through Finite Element Analysis. IECM [online]. 2016, 2016, 587-593 [cit. 2016-10-23].
- [10] BIANCHI, N. Synchronous reluctance and interior permanent magnet motors. In: 2013 IEEE Workshop on Electrical Machines Design, Control and Diagnosis (WEMDCD) [online]. IEEE, 2013, s. 75-84 [cit. 2016-11-10]. DOI: 10.1109/WEMDCD.2013.6525167. ISBN 978-1-4673-5658-9. Dostupné z: <http://ieeexplore.ieee.org/document/6525167/>
- [11] VÍCHA, Adam. Vlivy výrobních tolerancí permanentních magnetů na synchronní motory s permanentními magnety. Vysoké učení technické v Brně. Fakulta elektrotechniky a komunikačních technologií, 2016.
- [12] COENEN, I., M. VAN DER GIET a K. HAMEYER. Manufacturing Tolerances: Estimation and Prediction of Cogging Torque Influenced by Magnetization Faults. IEEE Transactions on Magnetics [online]. 2012, 48(5), 1932-1936 [cit. 2016-12-10]. DOI: 10.1109/TMAG.2011.2178252. ISSN 0018-9464. Dostupné z: <http://ieeexplore.ieee.org/document/6096415/>
- [13] BIANCHI, Nicola. Electrical machine analysis using finite elements. Boca Raton, FL: Talor & Francis, c2005. ISBN 0849333997.
- [14] ProFEMAG [online]. Switzerland [cit. 2016-12-10]. Dostupné z: https://www.profemag.ch/index.php?option=com_content&view=categories&id=19&Itemid=137
- [15] LUA-script [online]. [cit. 2016-12-10]. Dostupné z: <https://www.lua.org/about.html>
- [16] FURLAN, Ivano, Tomas PRADELLA a Massimo BARCARO. Low-torque ripple design of a ferrite-assisted synchronous reluctance motor. IET Electric Power Applications [online]. 2016, 10(5), 319-329 [cit. 2016-12-12]. DOI: 10.1049/iet-epa.2015.0248. ISSN 1751-8660. Dostupné z: <http://digital-library.theiet.org/content/journals/10.1049/iet-epa.2015.0248>
- [17] GUGLIELMI, Paolo, Barbara BOAZZO, Eric ARMANDO, Gianmario PELLEGRINO a Alfredo VAGATI. Permanent-Magnet Minimization in PM-Assisted Synchronous Reluctance Motors for Wide Speed Range. IEEE Transactions on Industry Applications [online]. 2013, 49(1), 31-41 [cit. 2016-12-12]. DOI: 10.1109/TIA.2012.2229372. ISSN 0093-9994. Dostupné z: <http://ieeexplore.ieee.org/document/6359898/>

- [18] VARTANIAN, Robert, Hamid A. TOLIYAT, Bilal AKIN a Richard POLEY. Power factor improvement of synchronous reluctance motors (SynRM) using permanent magnets for drive size reduction. In: 2012 Twenty-Seventh Annual IEEE Applied Power Electronics Conference and Exposition (APEC) [online]. IEEE, 2012, s. 628-633 [cit. 2016-12-12]. DOI: 10.1109/APEC.2012.6165884. ISBN 978-1-4577-1216-6. Dostupné z: <http://ieeexplore.ieee.org/document/6165884/>
- [19] BIANCHI, Nicola, Alessandro CASTAGNINI, Pietro Savio TERMINI a Giulio SECONDO. Fractional-slot PM assisted reluctance motors: Configuration comparison and optimization. In: 2016 XXII International Conference on Electrical Machines (ICEM) [online]. IEEE, 2016, s. 775-781 [cit. 2017-03-10]. DOI: 10.1109/ICELMACH.2016.7732614. ISBN 978-1-5090-2538-1. Dostupné z: <http://ieeexplore.ieee.org/document/7732614/>
- [20] BIANCHI, N., S. BOLOGNANI, M.D. PRE a G. GREZZANI. Design considerations for fractional-slot winding configurations of synchronous machines. IEEE Transactions on Industry Applications [online]. 2006, 42(4), 997-1006 [cit. 2017-04-29]. DOI: 10.1109/TIA.2006.876070. ISSN 0093-9994. Dostupné z: <http://ieeexplore.ieee.org/document/1658329/>
- [21] GERLACH, Tobias, Richard STECKEL, Thomas HUBERT a Andreas KREMSER. Eddy current loss analysis in permanent magnets of synchronous machines. In: 2016 6th International Electric Drives Production Conference (EDPC) [online]. IEEE, 2016, s. 246-252 [cit. 2017-04-30]. DOI: 10.1109/EDPC.2016.7851341. ISBN 978-1-5090-2908-2. Dostupné z: <http://ieeexplore.ieee.org/document/7851341/>
- [22] BALAMURALI, Aiswarya, Chunyan LAI, Voiko LOUKANOV a Narayan. C KAR. Modeling and analysis of carrier harmonic based eddy current losses in interior permanent magnet motors. In: 2016 IEEE Conference on Electromagnetic Field Computation (CEFC) [online]. IEEE, 2016, s. 1-1 [cit. 2017-04-30]. DOI: 10.1109/CEFC.2016.7816410. ISBN 978-1-5090-1032-5. Dostupné z: <http://ieeexplore.ieee.org/document/7816410/>
- [23] CHENG, Ming a Sa ZHU. Calculation of PM Eddy Current Loss in IPM Machine Under PWM VSI Supply With Combined 2-D FE and Analytical Method. IEEE Transactions on Magnetics [online]. 2017, 53(1), 1-12 [cit. 2017-04-30]. DOI: 10.1109/TMAG.2016.2611582. ISSN 0018-9464. Dostupné z: <http://ieeexplore.ieee.org/document/7572060/>
- [24] Ferrite Magnets/Ceramic Magnets Datasheet [online]. In: . s. 4 [cit. 2017-04-30]. Dostupné z: http://www.eclipsemagnetics.com/media/wysiwyg/datasheets/magnet_materials_and_assemblies/ferrite_magnets-ceramic_magnets_datasheet_v1.pdf

- [25] Classes of Magnetic Materials [online]. In: . University of Minnesota, College of Science and Engineering, s. 4 [cit. 2017-04-30]. Dostupné z: http://www.irm.umn.edu/hg2m/hg2m_b/hg2m_b.html#ferrimagnetism
- [26] MAXWELL, L. R. What is ferrimagnetism? Electrical Engineering [online]. 1954, 73(9), 804-806 [cit. 2017-05-01]. DOI: 10.1109/EE.1954.6438974. ISSN 0095-9197. Dostupné z: <http://ieeexplore.ieee.org/document/6438974/>
- [27] CELIE, Jonas, Marnix STIE, Jan RENS a Peter SERGEANT. Effects of cutting and annealing of amorphous materials for high speed permanent magnet machines. In: 2016 XXII International Conference on Electrical Machines (ICEM) [online]. IEEE, 2016, s. 1630-1635 [cit. 2017-05-01]. DOI: 10.1109/ICELMACH.2016.7732742. ISBN 978-1-5090-2538-1. Dostupné z: <http://ieeexplore.ieee.org/document/7732742/>
- [28] BIANCHI, Nicola, Silverio BOLOGNANI, Diego BON a Michele DAI PRE. Rotor Flux barrier Design for Torque Ripple Reduction in Synchronous Reluctance and PM-Assisted Synchronous Reluctance Motors. IEEE Transactions on Industry Applications [online]. 2009, 45(3), 921-928 [cit. 2017-05-19]. DOI: 10.1109/TIA.2009.2018960. ISSN 0093-9994. Dostupné z: <http://ieeexplore.ieee.org/document/4957501/>
- [29] M330-35A electrical steel datasheet. Cogent power [online]. [cit. 2017-05-19]. Dostupné z: <https://cogent-power.com/cms-data/downloads/m330-35a.pdf>

List of symbols, quantity a acronyms

PMSM	-	permanent magnet synchronous motor
AC	-	alternative current
SRM	-	synchronous reluctance machine motor
PM	-	permanent magnet
FEM	-	finite element method
FEA	-	finite element analysis
IPM	-	interior permanent magnet
SMPM	-	surface mounted permanent magnet
μ_r	-	relative permeability [-]
R_m	-	magnetic reluctance [Ω]
μ_0	-	permeability of vacuum [$H \cdot m^{-1}$]
l	-	length [m]
S	-	surface area [m^2]
L_a	-	inductance [H]
cos	-	goniometric function
L_{am}	-	maximal inductance [H]
M_{im}	-	developed electromagnetic torque [Nm]
W_m	-	magnetic energy [J]
sin	-	goniometric function
u_s	-	stator voltage [V]
u_d	-	Voltage in d-axis [V]
u_q	-	Voltage in q-axis [V]
i_s	-	stator current [V]
i_d	-	current in d-axis [V]
i_q	-	current in q-axis [V]
ω	-	Electrical speed [$rad \cdot s^{-1}$]
ω_{mech}	-	Mechanical speed [$rad \cdot s^{-1}$]
R_d	-	Resistance in d-axis [Ω]
R_q	-	Resistance in q-axis [Ω]
ψ_d	-	Magnetic flux linkage in d-axis [Wb]
ψ_q	-	Magnetic flux linkage in q-axis [Wb]
ψ_{PM}	-	PM magnetic flux linkage [Wb]

L_d	-	Inductance in d-axis [H]
L_q	-	Inductance in q-axis [H]
p	-	Number of pole pairs [-]
J	-	Moment of inertia [kg/m ²]
Ψ_{sm}	-	Magnetic flux linkage amplitude in d-axis [Wb]
Ψ_{dm}	-	Magnetic flux linkage amplitude in d-axis [Wb]
Ψ_{qm}	-	Magnetic flux linkage amplitude in q-axis [Wb]
$\Psi_{PM,m}$	-	PM magnetic flux linkage amplitude [Wb]
K_s	-	Electrical loading [A/m]
ϑ_s	-	Coordinate in mechanical degrees in stator reference frame [°mech]
ϑ_m	-	Angular position of the rotor in mechanical degrees [°mech]
α_i^e	-	Current phase in electrical degrees [°el]
t	-	Time [s]
k_{wn}	-	Winding factor of the n-th harmonic order [-]
N_s	-	Number of conductors per phase [-]
D	-	Inner stator diameter [m]
U_{ms}	-	Stator magnetic voltage [A]
ϑ_r	-	Coordinate in electrical degrees in rotor reference frame [°el]
ϕ_{PM1}	-	PM magnetic flux [Wb]
ϕ_{PM2}	-	PM magnetic flux [Wb]
B_{PM}	-	PM residual induction [T]
h_{PM1}	-	PM height [mm]
h_{PM2}	-	PM height [mm]
H_{cPM}	-	Coercive force [A/m]
U_{mr}	-	Rotor magnetic voltage [A]
U_{mr1}	-	Rotor magnetic voltage [A]
U_{mr2}	-	Rotor magnetic voltage [A]
U_{mag}	-	Air gap magnetic voltage [A]
t_b	-	Flux barrier thickness [mm]
l_b	-	Flux barrier length
l_{fe}	-	Stack length [mm]
ϕ_{g1}	-	Air gap magnetic flux [Wb]
ϕ_{g2}	-	Air gap magnetic flux [Wb]
ϕ_{g3}	-	Air gap magnetic flux [Wb]

g	-	Air gap length [mm]
R_{b1}	-	Flux barriers reluctance [H^{-1}]
R_{b2}	-	Flux barriers reluctance [H^{-1}]
ϑ_b	-	Half pole angle of flux barriers [$^\circ$]
ϑ_{b1}	-	Half pole angle of flux barriers [$^\circ$]
ϑ_{b2}	-	Half pole angle of flux barriers [$^\circ$]
a,b,c,d	-	Dimensionless coefficients for mag. voltage calculation [-]
M_{ag}	-	Air gap torque [Nm]
k_{PM1}	-	PM contribution [A]
k_{PM2}	-	PM contribution [A]
k_T	-	Torque constant [Hm]
λ_n, λ_m	-	Coefficients replacing forms in bracket [$^\circ mech$]
α_1, α_2	-	Coefficients replacing forms in bracket [$^\circ el$]
n,m	-	Orders of harmonic [-]
M_{avg}	-	Average torque [Nm]
M_{PP}	-	Torque ripple [%]
THD_{LL}	-	Total harmonic distortion [%]
$\cos \varphi$	-	power factor [-]
η	-	Efficiency [%]
ξ	-	Magnetic saliency [-]
A_{PM}	-	Permanent magnet area [mm^2]
PA	-	parametric analysis
q	-	number of slots per pole per phase [-]
$k_{p,Cu}$	-	slot copper fill factor [-]
l_b	-	stator coil overlap [mm]
I_S	-	stator coil current [A]
ϑ_{PM}	-	permanent magnet temperature [$^\circ C$]
MMF	-	Magnetomotive force [A]
σ	-	Equivalent stress [N/ mm^2 , MPa]
σ_{max}	-	Maximum yield strength [N/ mm^2 , MPa]

Attachments

Tab. (A1) - Results of the PA done on 12/10 combination with one flux barrier per pole

Model			Initial	Optimal
	Symbol	Unit		
Optimized parameter	d_bx1/d_by1	[mm/mm]	15/10	10/0
Average torque	M_{avg}	[Nm]	4.2	4.7
Torque ripple	M_{PP}	[%]	15.6	14.8
Terminal voltage	U_1	[V]	197.77	169.3
Total harmonic distortion	THD_{LL}	[%]	21.9	27.2
Power factor	$\cos \varphi$	[-]	0.415	0.542
Efficiency	η	[%]	89.81	92.06
Direct axis inductance	L_d	[mH]	41.15	35.88
Quadrature axis ind.	L_q	[mH]	21.52	17.7
Magnetic saliency	ξ	[-]	1.9	2
PM area	A_{PM}	[mm ²]	356.9	484.1

Tab. (A2) - Results of the first PA done on 12/10 combination with two flux barriers per pole

Model			Initial	Optimal
	Symbol	Unit		
Optimized parameter	d_bx1/d_by1	[mm/mm]	0/0	5/0
Average torque	M_{avg}	[Nm]	4.129	4.069
Torque ripple	M_{PP}	[%]	20.19	16.24
Terminal voltage	U_1	[V]	190.13	173.55
Total harmonic distortion	THD_{LL}	[%]	18.27	17.67
Power factor	$\cos \varphi$	[-]	0.428	0.461
Efficiency	η	[%]	90.46	91.07
Direct axis inductance	L_d	[mH]	39.66	36.42
Quadrature axis ind.	L_q	[mH]	19.47	18.04
Magnetic saliency	ξ	[-]	2	2
PM area	A_{PM}	[mm ²]	503.1	600.6

Tab. (A3) - Results of the second PA done on 12/10 combination with two flux barriers per pole

Model			Initial	Optimal
	Symbol	Unit		
Optimized parameter	q_bar/a_bar	[-/-]	1/1	0.8/1
Average torque	M_{avg}	[Nm]	4.069	4.047
Torque ripple	M_{PP}	[%]	16.24	15.23
Terminal voltage	U_1	[V]	173.55	165.92
Total harmonic distortion	THD_{LL}	[%]	17.67	17.53
Power factor	$\cos \varphi$	[-]	0.461	0.48
Efficiency	η	[%]	91.07	91.34
Direct axis inductance	L_d	[mH]	36.42	34.92
Quadrature axis ind.	L_q	[mH]	18.04	16.97
Magnetic saliency	ξ	[-]	2	2.1
PM area	A_{PM}	[mm ²]	600.6	587.4

Tab. (A4) - Results of the PA done on 27/6 combination with one flux barrier per pole

Model			Initial = Optimal
	Symbol	Unit	
Optimized parameter	d_bx1/d_by1	[mm/mm]	-7.5/-7.5
Average torque	M_{avg}	[Nm]	7.37
Torque ripple	M_{PP}	[%]	2.34
Terminal voltage	U_1	[V]	189.47
Total harmonic distortion	THD_{LL}	[%]	3
Power factor	$\cos \varphi$	[-]	0.75
Efficiency	η	[%]	94.17
Direct axis inductance	L_d	[mH]	71.26
Quadrature axis ind.	L_q	[mH]	23.27
Magnetic saliency	ξ	[-]	3.1
PM area	A_{PM}	[mm ²]	750

Tab. (A5) - Results of the first PA done on 27/6 combination with two flux barriers per pole

Model			Initial	Optimal
	Symbol	Unit		
Optimized parameter	d_{bx1}/d_{by1}	[mm/mm]	0/0	5/0
Average torque	M_{avg}	[Nm]	7.3	7.275
Torque ripple	M_{PP}	[%]	5.8	4.5
Terminal voltage	U_1	[V]	174.11	169.68
Total harmonic distortion	THD_{LL}	[%]	3.7	3.2
Power factor	$\cos \varphi$	[-]	0.702	0.717
Efficiency	η	[%]	94.09	94.09
Direct axis inductance	L_d	[mH]	49.18	51.35
Quadrature axis ind.	L_q	[mH]	7.02	8.75
Magnetic saliency	ξ	[-]	7	5.9
PM area	A_{PM}	[mm ²]	1098.7	898

Tab. (A6) - Results of the second PA done on 27/6 combination with two flux barriers per pole

Model			Initial	Optimal
	Symbol	Unit		
Optimized parameter	q_{bar}/a_{bar}	[-/-]	1/1	1/1.2
Average torque	M_{avg}	[Nm]	7.275	7.255
Torque ripple	M_{PP}	[%]	4.5	2.95
Terminal voltage	U_1	[V]	169.68	170.04
Total harmonic distortion	THD_{LL}	[%]	3.2	2.8
Power factor	$\cos \varphi$	[-]	0.717	0.714
Efficiency	η	[%]	94.09	94.08
Direct axis inductance	L_d	[mH]	51.35	51.5
Quadrature axis ind.	L_q	[mH]	8.75	8.84
Magnetic saliency	ξ	[-]	5.9	5.8
PM area	A_{PM}	[mm ²]	898	876.5

Tab. (A7) - Results of the PA done on 27/6 combination with three flux barriers per pole

Model			Initial = Optimal
	Symbol	Unit	
Optimized parameter	d_bx1/d_by1	[mm/mm]	0/0
Average torque	M_{avg}	[Nm]	4.615
Torque ripple	M_{PP}	[%]	13.53
Terminal voltage	U_1	[V]	196.94
Total harmonic distortion	THD_{LL}	[%]	21.4
Power factor	$\cos \varphi$	[-]	0.763
Efficiency	η	[%]	93.94
Direct axis inductance	L_d	[mH]	47.05
Quadrature axis ind.	L_q	[mH]	8.67
Magnetic saliency	ξ	[-]	5.4
PM area	A_{PM}	[mm ²]	1077.4

Tab. (A8) - Results of the PA done on 36/8 combination with one flux barrier per pole

Model			Initial	Optimal
	Symbol	Unit		
Optimized parameter	d_bx1/d_by1	[mm/mm]	0/0	-2.5/-5
Average torque	M_{avg}	[Nm]	7.2	8.1
Torque ripple	M_{PP}	[%]	12	3.5
Terminal voltage	U_1	[V]	192.88	186.4
Total harmonic distortion	THD_{LL}	[%]	7.1	2.4
Power factor	$\cos \varphi$	[-]	0.634	0.735
Efficiency	η	[%]	92.11	93.1
Direct axis inductance	L_d	[mH]	47.38	45.6
Quadrature axis ind.	L_q	[mH]	15.54	15.53
Magnetic saliency	ξ	[-]	3	2.9
PM area	A_{PM}	[mm ²]	479.2	729.5

Tab. (A9) - Results of the first PA done on 36/8 combination with two flux barriers per pole

Model			Initial	Optimal
	Symbol	Unit		
Optimized parameter	d_{bx1}/d_{by1}	[mm/mm]	0/0	10/5
Average torque	M_{avg}	[Nm]	8.175	7.971
Torque ripple	M_{PP}	[%]	3.7	3.3
Terminal voltage	U_1	[V]	186.36	182.9
Total harmonic distortion	THD_{LL}	[%]	4.8	2.2
Power factor	$\cos \varphi$	[-]	0.737	0.733
Efficiency	η	[%]	93.24	93.15
Direct axis inductance	L_d	[mH]	45.57	44.75
Quadrature axis ind.	L_q	[mH]	10.26	10.07
Magnetic saliency	ξ	[-]	4.4	4.4
PM area	A_{PM}	[mm ²]	867.8	808.5

Tab. (A10) - Results of the second PA done on 36/8 combination with two flux barriers per pole

Model			Initial	Optimal
	Symbol	Unit		
Optimized parameter	q_{bar}/a_{bar}	[-/-]	1/1	1/1.2
Average torque	M_{avg}	[Nm]	7.971	7.957
Torque ripple	M_{PP}	[%]	3.3	2.8
Terminal voltage	U_1	[V]	182.9	183.71
Total harmonic distortion	THD_{LL}	[%]	2.2	2.3
Power factor	$\cos \varphi$	[-]	0.733	0.729
Efficiency	η	[%]	93.15	93.15
Direct axis inductance	L_d	[mH]	44.75	44.98
Quadrature axis ind.	L_q	[mH]	10.07	7.86
Magnetic saliency	ξ	[-]	4.4	5.7
PM area	A_{PM}	[mm ²]	808.5	787.6

Tab. (A11) - Results of the PA done on 36/8 combination with three flux barriers per pole

Model			Initial = Optimal
	Symbol	Unit	
Optimized parameter	d _{bx1} /d _{by1}	[mm/mm]	0/0
Average torque	M _{avg}	[Nm]	7.982
Torque ripple	M _{pp}	[%]	16.9
Terminal voltage	U ₁	[V]	179.32
Total harmonic distortion	THD _{LL}	[%]	11.3
Power factor	cos φ	[-]	0.748
Efficiency	η	[%]	93.18
Direct axis inductance	L _d	[mH]	43.78
Quadrature axis ind.	L _q	[mH]	10.3
Magnetic saliency	ξ	[-]	4.2
PM area	A _{PM}	[mm ²]	950.6

Tab. (A12) - Results of the first PA done on 36/8 combination with two flux barriers per pole

Model			Initial	Optimal
	Symbol	Unit		
Optimized parameter	g _{2_bar} /g _{4_bar}	[mm/mm]	2.1/1.6	1.9/1.2
Average torque	M _{avg}	[Nm]	6.235	6.434
Torque ripple	M _{pp}	[%]	14.8	16
Terminal voltage	U ₁	[V]	155.84	165.41
Total harmonic distortion	THD _{LL}	[%]	12.3	10.1
Power factor	cos φ	[-]	0.772	0.751
Efficiency	η	[%]	94.11	94.13
Direct axis inductance	L _d	[mH]	47.83	50.86
Quadrature axis ind.	L _q	[mH]	10.7	10.75
Magnetic saliency	ξ	[-]	4.5	4.7
PM area	A _{PM}	[mm ²]	864	864

Tab. (A13) - Results of the first PA done on 36/8 combination with two flux barriers per pole

Model			Initial	Optimal
	Symbol	Unit		
Optimized parameter	d2_bar/d4_bar	[mm/mm]	1.6/0.8	2/1.2
Average torque	M_{avg}	[Nm]	6.434	6.538
Torque ripple	M_{PP}	[%]	16	12.4
Terminal voltage	U_1	[V]	165.41	166.87
Total harmonic distortion	THD_{LL}	[%]	10.1	8.6
Power factor	$\cos \varphi$	[-]	0.751	0.756
Efficiency	η	[%]	94.13	94.23
Direct axis inductance	L_d	[mH]	50.86	51.3
Quadrature axis ind.	L_q	[mH]	10.75	10.78
Magnetic saliency	ξ	[-]	4.7	4.8
PM area	A_{PM}	[mm ²]	864	864

Tab. (A14) - Results of the third PA done on 36/8 combination with two flux barriers per pole

Model			Initial	Optimal
	Symbol	Unit		
Optimized parameter	h1_bar/h2_bar	[mm/mm]	2/2	2.25/1.75
Average torque	M_{avg}	[Nm]	6.538	6.597
Torque ripple	M_{PP}	[%]	12.4	8.2
Terminal voltage	U_1	[V]	166.87	169.84
Total harmonic distortion	THD_{LL}	[%]	8.6	8.0
Power factor	$\cos \varphi$	[-]	0.756	0.750
Efficiency	η	[%]	94.23	94.25
Direct axis inductance	L_d	[mH]	51.3	52.23
Quadrature axis ind.	L_q	[mH]	10.78	11.21
Magnetic saliency	ξ	[-]	4.8	4.7
PM area	A_{PM}	[mm ²]	864	864

Tab. (A15) - Results of the fourth PA done on 36/8 combination with two flux barriers per pole

Model			Initial	Optimal
	Symbol	Unit		
Optimized parameter	a1/a2/a3/a4_bar	[mm/mm/mm/mm]	1,4/1,1/0,9/0,5	1,4/1,1/0,9/0,1
Average torque	M_{avg}	[Nm]	6.597	6.597
Torque ripple	M_{PP}	[%]	8.2	8.0
Terminal voltage	U_1	[V]	169.84	169.8
Total harmonic distortion	THD_{LL}	[%]	8.0	8.2
Power factor	$\cos \varphi$	[-]	0.750	0.750
Efficiency	η	[%]	94.25	94.24
Direct axis inductance	L_d	[mH]	52.23	52.21
Quadrature axis ind.	L_q	[mH]	11.21	10.97
Magnetic saliency	ξ	[-]	4.7	4.8
PM area	A_{PM}	[mm ²]	864	864

Tab. (A16) - Results of the first SRAM3 PA done on 36/8 combination

Model			Initial	Optimal
	Symbol	Unit		
Optimized parameter	b1_bar/b2_bar	[mm/mm]	16/10	18/16
Average torque	M_{avg}	[Nm]	5.970	5,986
Torque ripple	M_{PP}	[%]	7.68	4,48
Terminal voltage	U_1	[V]	178.33	183,09
Total harmonic distortion	THD_{LL}	[%]	9.2	8,6
Power factor	$\cos \varphi$	[-]	0,651	0,637
Efficiency	η	[%]	92,81	92,74
Direct axis inductance	L_d	[mH]	50,66	51,99
Quadrature axis ind.	L_q	[mH]	20,06	21,25
Magnetic saliency	ξ	[-]	2,5	2,4
PM area	A_{PM}	[mm ²]	495,6	495,6

Tab. (A17) - Results of the second SRAM3 PA done on 36/8 combination

Model			Initial	Optimal
	Symbol	Unit		
Optimized parameter	d1_bar/d2_bar	[mm/mm]	5/1.5	10/0,5
Average torque	M_{avg}	[Nm]	5,986	5,933
Torque ripple	M_{PP}	[%]	4,48	4,34
Terminal voltage	U_1	[V]	183,09	182,59
Total harmonic distortion	THD_{LL}	[%]	8,6	8,5
Power factor	$\cos \varphi$	[-]	0,637	0,633
Efficiency	η	[%]	92,74	92,73
Direct axis inductance	L_d	[mH]	51,99	51,83
Quadrature axis ind.	L_q	[mH]	21,25	19,84
Magnetic saliency	ξ	[-]	2,4	2,6
PM area	A_{PM}	[mm ²]	495,6	495,6

Tab. (A18) - Measuring equipment

Test equipment	Description	Type	Serial number
001008	Test bench	GNA200	Not available
003006	Oscilloscope	DL1520	7015GC701L
006008	Temperature data logger	OM TC-08	AO 017/798
016008	Resistance measuring device	Metrel MI 3210 10A	15410591
081005	Differential scanning head	SI 9110	70845
082006	Current clamps	C160	P01120308
091006	Power meter	Hioki 9193	941442